Nucl. Fusion **52** (2012) 123018 (24pp) doi:10.1088/0029-5515/52/12/123018

Toroidal current profile control during low confinement mode plasma discharges in DIII-D via first-principles-driven model-based robust control synthesis

Justin E. Barton[1], Mark D. Boyer[1], Wenyu Shi[1], Eugenio Schuster[1], Tim C. Luce[2], John R. Ferron[2], Michael L. Walker[2], David A. Humphreys[2], Ben G. Penaflor[2] and Robert D. Johnson[2]

[1] Department of Mechanical Engineering and Mechanics, Lehigh University, 19 Memorial Drive West, Bethlehem, PA 18015, USA
[2] General Atomics, 3550 General Atomics Court, San Diego, CA 92121, USA

E-mail: justin.barton@lehigh.edu

Received 9 April 2012, accepted for publication 20 September 2012
Published 26 November 2012
Online at stacks.iop.org/NF/52/123018

Abstract
In order for ITER to be capable of operating in advanced tokamak operating regimes, characterized by a high fusion gain, good plasma confinement, magnetohydrodynamic stability and a non-inductively driven plasma current, for extended periods of time, several challenging plasma control problems still need to be solved. Setting up a suitable toroidal current density profile in the tokamak is key for one possible advanced operating scenario characterized by non-inductive sustainment of the plasma current. At the DIII-D tokamak, the goal is to create the desired current profile during the ramp-up and early flat-top phases of the plasma discharge and then actively maintain this target profile for the remainder of the discharge. The evolution in time of the toroidal current profile in tokamaks is related to the evolution of the poloidal magnetic flux profile, which is modelled in normalized cylindrical coordinates using a first-principles, nonlinear, dynamic partial differential equation (PDE) referred to as the magnetic diffusion equation. The magnetic diffusion equation is combined with empirical correlations developed from physical observations and experimental data from DIII-D for the electron temperature, the plasma resistivity and the non-inductive current drive to develop a simplified, control-oriented, nonlinear, dynamic PDE model of the poloidal flux profile evolution valid for low confinement mode discharges. In this work, we synthesize a robust feedback controller to reject disturbances and track a desired reference trajectory of the poloidal magnetic flux gradient profile by employing the control-oriented model of the system. A singular value decomposition of the static gain matrix of the plant model is utilized to identify the most relevant control channels and is combined with the dynamic response of system around a given operating trajectory to design the feedback controller. A general framework for real-time feedforward + feedback control of magnetic and kinetic plasma profiles was implemented in the DIII-D Plasma Control System and was used to demonstrate the ability of the feedback controller to control the toroidal current profile evolution in the DIII-D tokamak. These experiments constitute the first time ever a first-principles-driven, model-based, closed-loop magnetic profile controller was successfully implemented and tested in a tokamak device.

(Some figures may appear in colour only in the online journal)

1. Introduction

The ITER project is attempting to prove the scientific feasibility of a commercial nuclear fusion tokamak power plant. However, in order for ITER to be successful, there are several challenging plasma control problems that still need to be solved. One of these challenges is the ability to operate the tokamak machine for sufficiently long plasma discharges. In response to this need, extensive research has been conducted to find so-called advanced tokamak (AT) operating scenarios [1] that are characterized by a high fusion gain, good plasma confinement, magnetohydrodynamic stability, and a non-inductively driven plasma current with a dominant fraction coming from the self-generated bootstrap current. If these

performance objectives are achieved, the cost and size of fusion reactors could be greatly reduced, and the machine could potentially be operated in a steady-state manner.

One possible advanced operating scenario is related to setting up a suitable toroidal current density profile in the machine that is characterized by a safety factor, or q, profile with a weakly reversed magnetic shear. Advances in current profile control at the JET and DIII-D tokamaks can be found in [2–5]. Also, profile control at the Tore Supra and JT-60U tokamaks is discussed in [6–8]. Experiments at the DIII-D tokamak focus on creating the desired current profile during the ramp-up and early flat-top phases of the plasma current evolution with the goal of actively maintaining this target profile throughout the remainder of the discharge. During the initial phase of the discharge, feedback control of $q(0, t)$ and $q_{\min}(t)$ has been demonstrated at DIII-D [5] by changing the plasma conductivity through electron heating. The employed controller requests a power level to the actuator, either electron cyclotron heating (ECH) or neutral beam injection (NBI), that is equal to a preprogrammed feedforward value plus the error in q times a proportional gain. The q profile is obtained in real-time from the motional Stark effect (MSE) diagnostic measurement. If the sampling rate of the q profile is reduced, because the MSE beam is modulated rather than run continuously, the closed-loop system has been observed to become unstable causing the q profile to oscillate. This behaviour, along with the strong coupling between the magnetic and kinetic plasma profiles and the high dimensionality of the problem when the objective is the control of the entire q profile and not only $q(0, t)$ and $q_{\min}(t)$, motivates the design of a model-based controller. By embedding the physics of the system, which can be captured by a control-oriented dynamic model, as well as the information on the diagnostic sampling rate into the control design process, a model-based controller can take into account the dynamics of the entire q profile in response to the available actuators, thus eliminating the need for trial-and-error tuning as a natural consequence and increasing the potential for improved performance. Progress towards control-oriented modelling of the current density profile, following both data-driven [4, 9] and first-principles-driven [10, 11] approaches, has been recently reported.

By following a data-driven modelling approach, linear, dynamic, plasma profile response models were recently obtained from experimental data by performing system identification experiments in JET [4], JT-60U and DIII-D [9]. The identified models were used to design controllers to simultaneously control magnetic and kinetic plasma profiles by exploiting the different time scales of the magnetic and kinetic variables. The proposed control architecture is two separate feedback loops that operate on the magnetic and kinetic time scales, respectively. The designed controllers use the heating and current drive systems to regulate the various plasma profiles around desired target profiles during the flat-top phase of the plasma discharge [4, 12, 13]. However, as the identified models are linear, they are only valid around the reference plasma state adopted during the system identification experiment. Therefore, the effectiveness of the controllers designed based on these models may be limited when the plasma state moves away from the reference state. Moreover, as these models are device-specific, dedicated system identification experiments are needed in each device, and potentially for each control scenario, to develop model-based controllers.

As an alternative to data-driven modelling, first-principles-driven modelling, and subsequent controller design, has the potential of overcoming these limitations. The first-principles-driven model has the advantages of being (i) extendable to various equilibrium configurations and operating scenarios, (ii) able to incorporate the nonlinear coupling between the various magnetic and kinetic plasma parameters and (iii) able to explicitly describe the temporal and spatial evolution of the current profile in response to nonlinear control actuation. The evolution of the toroidal current profile in tokamaks is related to the evolution of the poloidal magnetic flux profile, and in this work our focus is on the design of control schemes based on a first-principles-driven, control-oriented model of the poloidal flux profile evolution. The poloidal magnetic flux diffusion equation is derived from Gauss's law, Ampere's law, Faraday's law, Ohm's law and an equilibrium momentum balance. This model is combined with empirical correlations obtained from physical observations and experimental data for the electron temperature, the plasma resistivity, and the non-inductive current drive to obtain a simplified nonlinear, dynamic, control-oriented, partial differential equation (PDE) model describing the evolution of the poloidal magnetic flux profile in response to the electric field due to induction, the auxiliary heating and current drive systems and the line average plasma density in low confinement discharges [10]. The empirical laws employed for closure of the magnetic diffusion equation are based on general physical observations of the plasma response to the control actuators, which are not unique to any one machine. Since the laws have been observed in many machines, the first-principles-driven model can be adapted to any given tokamak by adjusting the constants and reference profiles in the empirical laws based on already existing experimental data from the tokamak of interest. Therefore, control strategies for various tokamaks operating in different equilibrium configurations can be synthesized from one model structure. In addition, first-principles-driven modelling provides the freedom of arbitrarily handling the trade-off between the simplicity of the model and both its physics accuracy and its range of validity, which will of course be reflected in the model-based controller's performance and capability.

The control strategy we employ to control the current profile evolution is a feedforward + feedback control scheme, where the feedforward controller is computed off-line and the feedback controller is computed on-line. Experiments have shown that some of the desired current profiles may not be achievable for all arbitrary initial conditions because the actuators used to manipulate the current profile evolution are physically constrained. The objective of the feedforward controller is to achieve the best possible q profile/target matching during the ramp-up and early flat-top phases of the plasma current evolution and to maintain it during the rest of the discharge. To add robustness to the control strategy, a feedback control input is added to the feedforward control input. In this work, we consider the problem of designing a feedback controller to track a desired reference trajectory of

the poloidal flux gradient profile, which is inversely related to the q profile. A general framework for real-time feedforward + feedback control of magnetic and kinetic plasma profiles was implemented in the DIII-D Plasma Control System (PCS) and was used to demonstrate the ability of the feedback controller to control the toroidal current profile evolution in the DIII-D tokamak. These experiments mark the first time ever a first-principles-driven, model-based, closed-loop magnetic profile controller was successfully implemented and tested in a tokamak device.

This paper is organized as follows. The current profile control problem during the various phases of the tokamak discharge is briefly described in section 2. In section 3, a simplified nonlinear, dynamic, control-oriented, PDE model for the evolution of the poloidal flux gradient profile valid for low confinement discharges is introduced. In the development of the control-oriented model, the non-inductive bootstrap current is neglected due to its effects being small in low confinement discharges, and the magnetic diffusion equation is combined with empirical correlations for the electron temperature, the plasma resistivity, and the non-inductive current drive developed from physical observations and experimental data from low confinement mode discharges in DIII-D. The governing infinite dimensional PDE is approximated by a finite dimensional system of ordinary differential equations to facilitate the synthesis of a feedback controller by employing a truncated Taylor series expansion in space. While the state of the reduced-order model is linearized around a given feedforward operating trajectory, the control input nonlinearities are preserved through a nonlinear transformation, and a time-varying state-space representation of the deviation dynamics is derived in section 4. In section 5, the time-varying state-space system is represented as an uncertain state-space model, i.e. a nominal time-invariant model plus a bounded uncertain component, which is then formulated into a robust control framework. The part of the plant output we can effectively control is determined by employing a singular value decomposition of the static gain matrix of the nominal plant model, which is combined with the dynamic response of the system around the given feedforward trajectory to synthesize a robust feedback controller. The feedback controller is synthesized by first considering the nominal model and then analyzing the stability of the closed-loop system in the presence of the model uncertainty. A general framework for real-time feedforward + feedback control of the magnetic and kinetic plasma profiles is implemented in the DIII-D PCS, and a simulation simserver (Simserver) that can interface with the DIII-D PCS is developed in section 6. In section 7 we test the feedback controller in Simserver simulations with the real-time code utilized in the DIII-D PCS, and in section 8 the feedback controller is tested in reference tracking and disturbance rejection experiments in the DIII-D tokamak. Finally, conclusions and future work are discussed in section 9.

2. Control problem description

The control objectives, as well as the dynamic models describing the time evolution of the toroidal current density profile, depend on the phase of the discharge. During the ramp-up phase and the first part of the flat-top phase, the plasma current is mainly driven by induction in both low confinement (L-mode) and high confinement (H-mode) plasma discharges. Therefore, the effect of the self-generated, non-inductive bootstrap current may be neglected in the formulation of the simplified PDE model of the system. The control goal for the initial phase of the discharge is to drive the poloidal flux gradient profile, which we denote as the variable θ, from an arbitrary initial condition to a predefined target profile. For the remainder of the flat-top phase of the discharge, the effect of the bootstrap current must be included in the dynamic model of the system for H-mode discharges but can still be neglected for L-mode discharges due to the bootstrap effects being small because of the lower temperature and density gradients in the plasma in this operating mode [14]. The control objective for this phase is to regulate the poloidal flux gradient profile around the achieved target profile with as little control effort as possible.

In this work, the focus is on the control objectives of the ramp-up and flat-top phases of the discharge in L-mode operating scenarios. The choice of L-mode operating scenarios rather than high performance H-mode operating scenarios is based on the fact that the coupling between the magnetic and kinetic plasma parameters is not as strong in this operating mode. As a result, the dynamics of the current profile evolution in L-mode are simplified, which reduces the complexity of the model-based control design process. Therefore, L-mode operating scenarios are more attractive for initial demonstration of the technical feasibility of controlling the current profile evolution in closed-loop experiments with controllers synthesized from first-principles-driven models. Once this methodology is validated, the focus will be on extending the approach to high performance H-mode scenarios by incorporating the effects of the bootstrap current in the first-principles-driven model of the system and synthesizing closed-loop controllers for this more complex operating mode.

The actuators we employ during the ramp-up and flat-top phases of the discharge to drive the poloidal flux gradient profile evolution $\theta(\hat{\rho}, t)$ to a desired target profile are the total plasma current, the total average NBI power and the line average plasma density. However, there is no guarantee that the desired target profile can be achieved for all arbitrary initial conditions due to (i) the nonlinear dynamics governing the evolution of the θ profile and (ii) the limitations of the control actuators to modify the evolution of the θ profile based on the physical design of the tokamak and the physical constraints in magnitude and rate of change of the actuators themselves. Therefore, an optimal control problem to determine control laws for the actuators that minimize the cost function

$$J = \int_{t_0}^{t_f} \frac{1}{N} \sum_{i=1}^{N} (\theta(\hat{\rho}_i, t) - \theta_{tar}(\hat{\rho}_i, t))^2 \mathrm{d}t \qquad (1)$$

must be solved, where t_0 and t_f are the beginning and ending times of the discharge, $\hat{\rho}$ denotes the normalized effective minor radius of the magnetic surface within the plasma, N is the number of discrete points used to specify the θ profile at the spatial locations $\hat{\rho}_i$, and $\theta_{tar}(\hat{\rho}_i)$ denotes the target profile. The control strategy we employ is a feedforward + feedback control scheme with the goal being to design the feedforward

controller based on the poloidal flux gradient profile evolution predicted by the PDE model such that (1) is minimized in the absence of external disturbances to the system for a given nominal initial condition. A control-oriented model of the poloidal flux profile evolution for L-mode plasma discharges was developed in [10]. During the ramp-up and early flat-top phases of L-mode operating scenarios, nonlinear programming [15] and extremum seeking [16] have been employed to solve the finite-time optimal control problem for the nonlinear PDE system to determine optimal feedforward control laws for the manipulated inputs. During normal tokamak operation, it is difficult to achieve a perfect matching of the nominal initial θ profile. In addition, the control-oriented model does not capture all of the physical phenomena that affect the θ profile evolution, therefore, the actual profile evolution in the tokamak will be different from the evolution predicted by the model. Therefore, the feedback controller is mounted on top of the feedforward controller to add robustness to the control scheme. The feedback controller is implemented with the goal of being able to track a desired reference trajectory of the poloidal flux gradient profile, account for the mismatch between the assumed and the actual initial condition, reject the effects of external disturbances to the system, and overcome the uncertainties in the model used for the control design. We now focus on the synthesis of a feedback controller to accomplish the aforementioned feedback control objectives.

3. First-principles-driven current profile evolution model

Any arbitrary quantity that is constant on each magnetic flux surface within the tokamak plasma can be used to index the magnetic flux surfaces. We choose the mean effective minor radius, ρ, of the magnetic flux surface, i.e. $\pi B_{\phi,0}\rho^2 = \Phi$, as the indexing variable, where Φ is the toroidal magnetic flux and $B_{\phi,0}$ is the reference magnetic field at the geometric major radius R_0 of the tokamak. The normalized effective minor radius is defined as $\hat{\rho} = \rho/\rho_b$, where ρ_b is the mean effective minor radius of the last closed magnetic flux surface. The evolution of the poloidal magnetic flux in normalized cylindrical coordinates is given by the magnetic diffusion equation [10, 17, 18]

$$\frac{\partial\psi}{\partial t} = \frac{\eta(T_e)}{\mu_0\rho_b^2\hat{F}^2}\frac{1}{\hat{\rho}}\frac{\partial}{\partial\hat{\rho}}\left(\hat{\rho}\hat{F}\hat{G}\hat{H}\frac{\partial\psi}{\partial\hat{\rho}}\right) + R_0\hat{H}\eta(T_e)\frac{\langle\bar{j}_{NI}\cdot\bar{B}\rangle}{B_{\phi,0}}, \quad (2)$$

where ψ is the poloidal stream function which is closely related to the poloidal flux Ψ, i.e. $\Psi = 2\pi\psi$, t is the time, η is the plasma resistivity, T_e is the electron temperature, μ_0 is the vacuum permeability, $\bar{j}_{NI}$ are the external sources of non-inductive current density (NBI, ECH, etc), $\bar{B}$ is the magnetic field and $\langle\rangle$ denotes a flux-surface average. The parameters $\hat{F}$, $\hat{G}$ and $\hat{H}$ are geometric factors of the DIII-D tokamak, which are functions of $\hat{\rho}$, and are given in [10] for a particular magnetic configuration. The boundary conditions are given by

$$\left.\frac{\partial\psi}{\partial\hat{\rho}}\right|_{\hat{\rho}=0} = 0 \qquad \left.\frac{\partial\psi}{\partial\hat{\rho}}\right|_{\hat{\rho}=1} = -\frac{\mu_0}{2\pi}\frac{R_0}{\hat{G}\Big|_{\hat{\rho}=1}\hat{H}\Big|_{\hat{\rho}=1}}I(t), \quad (3)$$

where $I(t)$ denotes the total plasma current.

In order to develop a control-oriented model of (2), simplified scenario-oriented models for the electron temperature, the plasma resistivity, and the non-inductive current density were determined from empirical correlations obtained from physical observations and experimental data from DIII-D for L-mode discharges [10]. The electron temperature is modelled as

$$T_e(\hat{\rho},t) = k_{T_e}T_e^{profile}(\hat{\rho})\frac{I(t)\sqrt{P_{tot}(t)}}{\bar{n}(t)}, \quad (4)$$

where k_{T_e} is a constant, $T_e^{profile}(\hat{\rho})$ is a reference electron temperature profile, $P_{tot}(t)$ is the total average neutral beam power and $\bar{n}(t)$ is the line average plasma density. The plasma current is mainly driven by induction during L-mode discharges, therefore, the effects of the bootstrap current on the evolution of the poloidal magnetic flux are neglected in the formulation of the model of the non-inductive current density, which is modelled as

$$\frac{\langle\bar{j}_{NI}\cdot\bar{B}\rangle}{B_{\phi,0}} = k_{NI_{par}}j_{NI_{par}}^{profile}(\hat{\rho})\frac{I(t)^{1/2}P_{tot}(t)^{5/4}}{\bar{n}(t)^{3/2}}, \quad (5)$$

where $k_{NI_{par}}$ is a constant and $j_{NI_{par}}^{profile}(\hat{\rho})$ is a reference non-inductive current deposition profile. The plasma resistivity $\eta(T_e)$ scales with the electron temperature as

$$\eta(\hat{\rho},t) = \frac{k_{eff}Z_{eff}}{T_e^{3/2}(\hat{\rho},t)}, \quad (6)$$

where k_{eff} is a constant and Z_{eff} is the effective average charge of the ions in the plasma, which is assumed constant in space and time. The reference profiles as well as the values of the constants are given in [10]. By using these simplified models, the evolution of the poloidal magnetic flux in normalized cylindrical coordinates is given by the magnetic diffusion equation

$$\frac{\partial\psi}{\partial t} = f_1(\hat{\rho})u_1(t)\frac{1}{\hat{\rho}}\frac{\partial}{\partial\hat{\rho}}\left(\hat{\rho}f_4(\hat{\rho})\frac{\partial\psi}{\partial\hat{\rho}}\right) + f_2(\hat{\rho})u_2(t) \quad (7)$$

with boundary conditions

$$\left.\frac{\partial\psi}{\partial\hat{\rho}}\right|_{\hat{\rho}=0} = 0 \qquad \left.\frac{\partial\psi}{\partial\hat{\rho}}\right|_{\hat{\rho}=1} = -k_3u_3(t), \quad (8)$$

where

$$f_1(\hat{\rho}) = \frac{k_{eff}Z_{eff}}{k_{T_e}^{3/2}\mu_0\rho_b^2\hat{F}^2(\hat{\rho})(T_e^{profile}(\hat{\rho}))^{3/2}},$$

$$f_2(\hat{\rho}) = \frac{k_{eff}Z_{eff}R_0k_{NI_{par}}\hat{H}(\hat{\rho})j_{NI_{par}}^{profile}(\hat{\rho})}{k_{T_e}^{3/2}(T_e^{profile}(\hat{\rho}))^{3/2}},$$

$$f_4(\hat{\rho}) = \hat{F}(\hat{\rho})\hat{G}(\hat{\rho})\hat{H}(\hat{\rho}) \qquad k_3 = \frac{\mu_0}{2\pi}\frac{R_0}{\hat{G}\Big|_{\hat{\rho}=1}\hat{H}\Big|_{\hat{\rho}=1}},$$

$$u_1(t) = \left(\frac{\bar{n}(t)}{I(t)\sqrt{P_{tot}(t)}}\right)^{3/2},$$

$$u_2(t) = \frac{\sqrt{P_{tot}(t)}}{I(t)} \qquad u_3(t) = I(t). \quad (9)$$

The magnetic diffusion equation (7) admits control through interior actuation via $u_2(t)$, through boundary actuation via $u_3(t)$, and through what we name diffusivity actuation in this work via $u_1(t)$. As the experiment and the equilibrium change, the constants k_{T_e} and $k_{\mathrm{NI}_{\mathrm{par}}}$, the reference profiles $T_e^{\mathrm{profile}}(\hat{\rho})$ and $j_{\mathrm{NI}_{\mathrm{par}}}^{\mathrm{profile}}(\hat{\rho})$ and the geometric factor profiles $\hat{F}(\hat{\rho})$, $\hat{G}(\hat{\rho})$ and $\hat{H}(\hat{\rho})$ will also change. Therefore, the dependence of the parameters f_1, f_2 and f_4 on $\hat{\rho}$ will change, but the structure of (7) and (8) will remain the same.

The control inputs $u_1(t)$, $u_2(t)$ and $u_3(t)$ of the magnetic diffusion equation have large order of magnitude differences which is not conducive to developing a feedback control algorithm that uses all of the available actuators to their fullest extent. Therefore, we normalize (7) by determining the maximum feedforward values of the three control inputs, which are denoted as $u_{1_{\mathrm{norm}}}$, $u_{2_{\mathrm{norm}}}$ and $u_{3_{\mathrm{norm}}}$, respectively. The control inputs are scaled as $u_1^{\mathrm{s}}(t) = u_1(t)/u_{1_{\mathrm{norm}}}$, $u_2^{\mathrm{s}}(t) = u_2(t)/u_{2_{\mathrm{norm}}}$ and $u_3^{\mathrm{s}}(t) = u_3(t)/u_{3_{\mathrm{norm}}}$, and the parameters in the governing PDE (7) are scaled as $f_1^{\mathrm{s}}(\hat{\rho}) = u_{1_{\mathrm{norm}}} f_1(\hat{\rho})$, $f_2^{\mathrm{s}}(\hat{\rho}) = u_{2_{\mathrm{norm}}} f_2(\hat{\rho})$ and $k_3^{\mathrm{s}} = u_{3_{\mathrm{norm}}} k_3$ where $(\cdot)^{\mathrm{s}}$ denotes a scaled quantity. Now each control input can vary between the same magnitude range, i.e. zero to one, and a feedback controller can be designed to use the full range of each actuator. The superscript s used to denote the scaled control inputs and equation parameters is dropped for the remainder of this paper in order to simplify notation.

The q profile, defined as $q(\hat{\rho}, t) = -\mathrm{d}\Phi/\mathrm{d}\Psi$, is related to the toroidal current profile in the machine [16]. By using the constant relationship between ρ and Φ, $\pi B_{\phi,0}\rho^2 = \Phi$, and the definition of $\hat{\rho}$, the safety factor is written as

$$q(\hat{\rho}, t) = -\frac{\mathrm{d}\Phi}{\mathrm{d}\Psi} = -\frac{\mathrm{d}\Phi}{2\pi\,\mathrm{d}\psi} = -\frac{\frac{\partial\Phi}{\partial\rho}\frac{\partial\rho}{\partial\hat{\rho}}}{2\pi\frac{\partial\psi}{\partial\hat{\rho}}} = -\frac{B_{\phi,0}\rho_b^2\hat{\rho}}{\partial\psi/\partial\hat{\rho}}. \quad (10)$$

Because the q profile is inversely dependent on the gradient of the poloidal stream function $\partial\psi/\partial\hat{\rho}$, it is chosen to be the controlled variable and is denoted by

$$\theta(\hat{\rho}, t) = \partial\psi/\partial\hat{\rho}(\hat{\rho}, t). \quad (11)$$

In order to obtain a PDE for $\theta(\hat{\rho}, t)$, (7) is expanded using the chain rule as

$$\frac{\partial\psi}{\partial t} = f_1 u_1(t)\frac{1}{\hat{\rho}}\left[\hat{\rho}\frac{\partial\psi}{\partial\hat{\rho}}\frac{\mathrm{d}f_4}{\mathrm{d}\hat{\rho}} + f_4\frac{\partial\psi}{\partial\hat{\rho}} + \hat{\rho}f_4\frac{\partial^2\psi}{\partial\hat{\rho}^2}\right] + f_2 u_2(t). \quad (12)$$

Inserting (11) into (12) results in the following PDE:

$$\frac{\partial\psi}{\partial t} = f_1(\hat{\rho})u_1(t)\frac{1}{\hat{\rho}}\left[\hat{\rho}\theta f_4'(\hat{\rho}) + f_4(\hat{\rho})\theta + \hat{\rho}f_4(\hat{\rho})\frac{\partial\theta}{\partial\hat{\rho}}\right] + f_2(\hat{\rho})u_2(t), \quad (13)$$

where $(\cdot)' = \mathrm{d}/\mathrm{d}\hat{\rho}$. By differentiating (13) with respect to $\hat{\rho}$, the PDE governing the evolution of $\theta(\hat{\rho}, t)$ is found to be

$$\frac{\partial\theta}{\partial t} = \left[h_0(\hat{\rho})\frac{\partial^2\theta}{\partial\hat{\rho}^2} + h_1(\hat{\rho})\frac{\partial\theta}{\partial\hat{\rho}} + h_2(\hat{\rho})\theta\right]u_1(t) + h_3(\hat{\rho})u_2(t) \quad (14)$$

with boundary conditions

$$\theta(0, t) = 0 \qquad \theta(1, t) = -k_3 u_3(t), \quad (15)$$

where

$$\begin{aligned} h_0(\hat{\rho}) &= f_1(\hat{\rho})f_4(\hat{\rho}),\\ h_1(\hat{\rho}) &= f_1'(\hat{\rho})f_4(\hat{\rho}) + f_1(\hat{\rho})f_4(\hat{\rho})/\hat{\rho} + 2f_1(\hat{\rho})f_4'(\hat{\rho}),\\ h_2(\hat{\rho}) &= f_1'(\hat{\rho})f_4'(\hat{\rho}) + f_1'(\hat{\rho})f_4(\hat{\rho})/\hat{\rho} + f_1(\hat{\rho})f_4'(\hat{\rho})/\hat{\rho}\\ &\quad - f_1(\hat{\rho})f_4(\hat{\rho})/\hat{\rho}^2 + f_1(\hat{\rho})f_4''(\hat{\rho}),\\ h_3(\hat{\rho}) &= f_2'(\hat{\rho}). \end{aligned} \quad (16)$$

The model (14)–(16) is the starting point for the development of the feedback controller design. This first-principles-driven, control-oriented, PDE model contains the physics information of how the dynamics of the poloidal flux gradient profile are influenced by the control actuators. The goal is to now convert the physics information contained in the model into a form suitable to synthesize a feedback controller, thus allowing the physics contained in the model to be embedded into the feedback controller.

4. Model reduction via truncated taylor series expansion

In order to facilitate the design of a feedback controller, the governing infinite dimensional PDE (14) is approximated by a finite dimensional system of ordinary differential equations (ODEs). This is accomplished by discretizing (14) in space by using a truncated Taylor series expansion to approximate the spatial derivatives while leaving the time domain continuous [19]. The non-dimensional spatial domain of interest, [0,1], is represented as l nodes, and the spacing between the nodes, $\Delta\hat{\rho}$, is defined as $\Delta\hat{\rho} = 1/(l-1)$. Central finite difference spatial derivative approximations of order $\Delta\hat{\rho}^2$ are used in the interior node region, $2 \leqslant i \leqslant (l-1)$. After applying the spatial derivative approximations to (14) and taking into account the boundary conditions (15), we obtain a matrix representation for the reduced-order model

$$\dot{\alpha}(t) = \Gamma\alpha(t)v_1(t) + \Omega v_2(t) + \Pi v_3(t), \quad (17)$$

where the vector $\alpha = [\theta_2, \ldots, \theta_{l-1}]^{\mathrm{T}} \in \mathbb{R}^{(l-2)\times 1}$ is the state of the system at the interior discrete nodes, the vector

$$[v_1(t), v_2(t), v_3(t)]^{\mathrm{T}} = [u_1(t), u_2(t), u_1(t)u_3(t)]^{\mathrm{T}} \in \mathbb{R}^{3\times 1} \quad (18)$$

is the control input, and $\Gamma \in \mathbb{R}^{(l-2)\times(l-2)}$, $\Omega \in \mathbb{R}^{(l-2)\times 1}$ and $\Pi \in \mathbb{R}^{(l-2)\times 1}$ are the system matrices. The system matrices for the interior node $i = 2$ are defined as

$$\begin{aligned} \Gamma_{1,1} &= h_2(\Delta\hat{\rho}) - \frac{2h_0(\Delta\hat{\rho})}{(\Delta\hat{\rho})^2} \qquad \Gamma_{1,2} = \frac{h_0(\Delta\hat{\rho})}{(\Delta\hat{\rho})^2} + \frac{h_1(\Delta\hat{\rho})}{2\Delta\hat{\rho}},\\ \Omega_1 &= h_3(\Delta\hat{\rho}) \qquad \Pi_1 = 0. \end{aligned} \quad (19)$$

The system matrices for the interior node region, $3 \leqslant i \leqslant (l-2)$, are defined as

$$\begin{aligned} \Gamma_{i-1,i-2} &= \frac{h_0(\Delta x)}{(\Delta\hat{\rho})^2} - \frac{h_1(\Delta x)}{2\Delta\hat{\rho}},\\ \Gamma_{i-1,i-1} &= h_2(\Delta x) - \frac{2h_0(\Delta x)}{(\Delta\hat{\rho})^2},\\ \Gamma_{i-1,i} &= \frac{h_0(\Delta x)}{(\Delta\hat{\rho})^2} + \frac{h_1(\Delta x)}{2\Delta\hat{\rho}},\\ \Omega_{i-1} &= h_3(\Delta x) \qquad \Pi_{i-1} = 0, \end{aligned} \quad (20)$$

where $\Delta x = (i-1)\Delta\hat{\rho}$. The system matrices for the interior node $i = l-1$ are defined as

$$\begin{aligned}\Gamma_{l-2,l-2} &= h_2(\Delta x^*) - \frac{2h_0(\Delta x^*)}{(\Delta\hat{\rho})^2},\\ \Gamma_{l-2,l-3} &= \frac{h_0(\Delta x^*)}{(\Delta\hat{\rho})^2} - \frac{h_1(\Delta x^*)}{2\Delta\hat{\rho}},\\ \Omega_{l-2} &= h_3(\Delta x^*),\\ \Pi_{l-2} &= -k_3\left(\frac{h_0(\Delta x^*)}{(\Delta\hat{\rho})^2} + \frac{h_1(\Delta x^*)}{2\Delta\hat{\rho}}\right),\end{aligned} \tag{21}$$

where $\Delta x^* = (l-2)\Delta\hat{\rho}$. All other entries in the Γ system matrix are zero. The values of θ at the boundary nodes $i = 1$ and $i = l$ are known from (15) and are therefore not included in the reduced-order model (17).

Let $\alpha_{\mathrm{FF}}(t)$ and $v_{\mathrm{FF}}(t)$ be the feedforward trajectories of the states and control inputs, respectively with initial condition $\alpha_{\mathrm{FF}}(0)$. These feedforward trajectories satisfy

$$\dot{\alpha}_{\mathrm{FF}}(t) = \Gamma\alpha_{\mathrm{FF}}(t)v_{1_{\mathrm{FF}}}(t) + \Omega v_{2_{\mathrm{FF}}}(t) + \Pi v_{3_{\mathrm{FF}}}(t). \tag{22}$$

By defining the perturbation variables $x(t) = \alpha(t) - \alpha_{\mathrm{FF}}(t)$ and $v_{\mathrm{FB}}(t) = v(t) - v_{\mathrm{FF}}(t)$, where $x(t)$ is the deviation away from the feedforward state trajectories and $v_{\mathrm{FB}}(t)$ is the output of the to-be-designed feedback controller, we can obtain a model suitable for tracking control design. Inserting the perturbation variables into (17) results in

$$\begin{aligned}\dot{\alpha}_{\mathrm{FF}} + \dot{x} = \Gamma\big(\alpha_{\mathrm{FF}} + x\big)\big(v_{1_{\mathrm{FF}}} + v_{1_{\mathrm{FB}}}\big) + \Omega\big(v_{2_{\mathrm{FF}}} + v_{2_{\mathrm{FB}}}\big)\\ + \Pi\big(v_{3_{\mathrm{FF}}} + v_{3_{\mathrm{FB}}}\big).\end{aligned} \tag{23}$$

By using (22), we can express (23) as

$$\dot{x} = \Gamma v_{1_{\mathrm{FF}}}x + \Gamma\big(\alpha_{\mathrm{FF}} + x\big)v_{1_{\mathrm{FB}}} + \Omega v_{2_{\mathrm{FB}}} + \Pi v_{3_{\mathrm{FB}}}. \tag{24}$$

Due to the term $\Gamma x v_{1_{\mathrm{FB}}}$, equation (24), which describes the behaviour of the deviation dynamics, is bilinear (nonlinearity resulting from the product between the control input and the state). In addition, the control inputs $v_{1_{\mathrm{FB}}}$, $v_{2_{\mathrm{FB}}}$ and $v_{3_{\mathrm{FB}}}$ are nonlinear functions of the real actuators as shown by the nonlinear transformations (9) and (18). While we neglect in this work the bilinear state behaviour by assuming that the feedback control input v_{FB} is able to keep the deviation of the system state away from the feedforward state trajectory small, i.e. $\alpha_{\mathrm{FF}} \gg x$, we preserve the dominant control input nonlinearities through the nonlinear transformations (9) and (18). An approximate linearization of the state dynamics can therefore be obtained by neglecting the nonlinear term, i.e.

$$\big(\alpha_{\mathrm{FF}} + x\big) \approx \alpha_{\mathrm{FF}}, \tag{25}$$

and rewriting (24) as

$$\dot{x} = \Gamma v_{1_{\mathrm{FF}}}x + \Gamma\alpha_{\mathrm{FF}}v_{1_{\mathrm{FB}}} + \Omega v_{2_{\mathrm{FB}}} + \Pi v_{3_{\mathrm{FB}}}. \tag{26}$$

Simulations and experiments show the closed-loop system to be robust to this approximation and indicate no need for the extra burden of taking into account the bilinear state behaviour during the control synthesis, which is indeed possible. The deviation dynamics (26) can be written as a linear, time-variant, dynamic, state-space model, i.e.

$$\begin{aligned}\dot{x} &= A(t)x + B(t)v_{\mathrm{FB}},\\ y &= Cx + Dv_{\mathrm{FB}},\end{aligned} \tag{27}$$

where $A(t) = \Gamma v_{1_{\mathrm{FF}}}(t) \in \mathbb{R}^{n\times n}$, $B(t) = [\Gamma\alpha_{\mathrm{FF}}(t), \Omega, \Pi] \in \mathbb{R}^{n\times 3}$, $C = I_n \in \mathbb{R}^{n\times n}$ where I_n is an $n\times n$ identity matrix, $D = 0 \in \mathbb{R}^{n\times 3}$, $x \in \mathbb{R}^{n\times 1}$, $y \in \mathbb{R}^{n\times 1}$, $v_{\mathrm{FB}} = [v_{1_{\mathrm{FB}}}, v_{2_{\mathrm{FB}}}, v_{3_{\mathrm{FB}}}]^{\mathrm{T}} \in \mathbb{R}^{3\times 1}$ and $n = l-2$. Here α, and therefore x, is assumed measurable. A linear control law for the inputs $v_{1_{\mathrm{FB}}}(t)$, $v_{2_{\mathrm{FB}}}(t)$ and $v_{3_{\mathrm{FB}}}(t)$ can now be determined and combined with the nonlinear inverse transformations resulting from (9) and (18) to produce an overall nonlinear control law for $I(t)$, $P_{\mathrm{tot}}(t)$ and $\bar{n}(t)$.

The first-principles-driven linear model for the deviation dynamics (27) is similar in structure to the linear plasma response models obtained by performing system identification experiments. However, there are some subtle differences between the two types of models. Firstly, the first-principles-driven deviation model can be obtained around any feedforward reference trajectory of the system while the data-driven deviation model can only be obtained around the reference plasma state adopted during the identification process. Secondly, the first-principles-driven deviation model is time varying, therefore, it provides information on how the deviation dynamics evolve throughout the discharge while the data-driven deviation model is time invariant. Finally, the first-principles-driven deviation model is able to capture the nonlinear effect the control actuators have on the current profile evolution through the transformations (9) and (18), while the data-driven deviation model can only capture the linear effect the control actuators have on the current profile evolution.

5. System manipulation into a control framework and feedback controller design

We now have a time-varying linear model describing the dynamic behaviour of the system around any given feedfoward operating trajectory that we can use to synthesize a feedback controller. However, most linear control design techniques are suited for time-invariant model dynamics, i.e. the state-space matrices A, B, C and D of the model are not a function of time. Therefore, we choose to model the time-varying system (27) as a nominal time-invariant model plus a bounded uncertain component. We then seek to design a feedback controller to stabilize the closed-loop system for all allowable uncertain perturbations, i.e. we follow what is called robust control design.

5.1. System model in robust control framework

The control inputs $v_{\mathrm{FF}}(t)$ are chosen to produce a desired trajectory of the system $\alpha_{\mathrm{FF}}(t)$ [15, 16], therefore, both time-varying quantities are bounded. We choose to model the time-varying parameters $v_{1_{\mathrm{FF}}}(t)$ and $\alpha_{\mathrm{FF}}(t)$ in the definition of the system matrices of (27) as a nominal value plus a bounded uncertain component, i.e.,

$$v_{1_{\mathrm{FF}}}(t) \in \gamma_v\Big(1 + \beta_v\delta_v\Big) \quad \alpha_{i_{\mathrm{FF}}}(t) \in \gamma_\alpha^i\Big(1 + \beta_\alpha^i\delta_\alpha^i\Big), \tag{28}$$

where $\gamma_v = (v_{1_{\mathrm{FF}_{\max}}} + v_{1_{\mathrm{FF}_{\min}}})/2$, $\gamma_\alpha^i = (\alpha_{i_{\mathrm{FF}_{\max}}} + \alpha_{i_{\mathrm{FF}_{\min}}})/2$, $\beta_v = (v_{1_{\mathrm{FF}_{\max}}} - v_{1_{\mathrm{FF}_{\min}}})/(2\gamma_v)$ and $\beta_\alpha^i = (\alpha_{i_{\mathrm{FF}_{\max}}} - \alpha_{i_{\mathrm{FF}_{\min}}})/(2\gamma_\alpha^i)$ with $|\delta_v| \leqslant 1$ and $|\delta_\alpha^i| \leqslant 1$ where $i = 1, 2, \ldots, n$. Since the vector α_{FF} contains the value of θ at the n nodes and

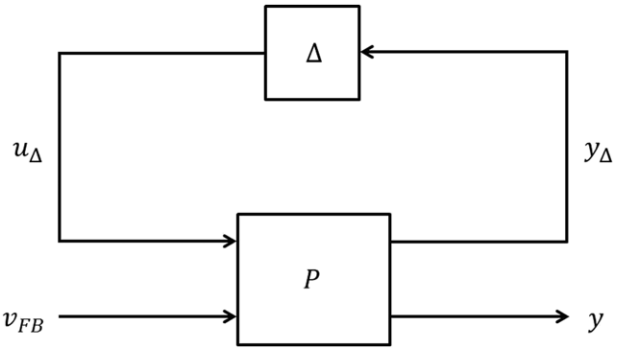

Figure 1. General control configuration with model uncertainty.

the parameter $v_{1_{FF}}$ is a scalar, this method of modelling the time-varying parameters produces $n+1$ uncertain parameters. By inserting the models (28) into (27) and defining the total uncertainty vector δ as $\delta = [\delta_\alpha^1, \ldots, \delta_\alpha^n, \delta_v] \in \mathbb{R}^{(n+1)\times 1}$, the state-space matrices $A(t)$, $B(t)$, C and D in (27) are expressed as

$$A(t) = A_0 + \sum_{m=1}^{n+1} \delta_m A_m^* \quad B(t) = B_0 + \sum_{m=1}^{n+1} \delta_m B_m^*,$$
$$C = C_0 + \sum_{m=1}^{n+1} \delta_m C_m^* \quad D = D_0 + \sum_{m=1}^{n+1} \delta_m D_m^*, \tag{29}$$

where

$$A_0 = \gamma_v \Gamma \qquad B_{0_k} = \left[\sum_{i=1}^{n} \gamma_\alpha^i \Gamma_{k,i}, \Omega_k, \Pi_k\right],$$
$$C_0 = I_n \qquad D_0 = 0 \tag{30}$$

and

$$A_{1,2,\ldots,n}^* = 0 \qquad A_{n+1}^* = \gamma_v \beta_v \Gamma,$$
$$B_{m_k}^* = \left[\left(\gamma_\alpha^m \beta_\alpha^m\right)\Gamma_{k,m}, 0, 0\right] \quad \text{for } m = 1, 2, \ldots, n$$
$$B_{n+1}^* = 0,$$
$$C_{1,2,\ldots,n+1}^* = 0 \qquad D_{1,2,\ldots,n+1}^* = 0, \tag{31}$$

where $k = 1, 2, \ldots, n$, $\Gamma_{k,i}$ denotes the kth row ith column component of Γ, B_{0_k} and $B_{m_k}^*$ denote the kth component of B_0 and B_m^*, respectively, and I_n denotes the $n \times n$ identity matrix. The state-space matrices A_0, B_0, C_0 and D_0 represent the nominal system, δ_m denotes the mth component of δ, and the state-space matrices A_m^*, B_m^*, C_m^* and D_m^* represent the influence that each uncertain parameter δ_m has on the system. See appendix A for a derivation of this model representation.

A linear system with state-space matrices A, B, C and D has a transfer function representation $G(s) = C(sI_n - A)^{-1}B + D$ that describes the relationship between the system's inputs and outputs, i.e. $y = G(s)v_{FB}$, where s denotes the Laplace variable and n is the number of states of the system. If we insert the representation of the state-space matrices (29) into the transfer function representation of the system, the nominal model will be coupled with the uncertain parameters δ_m for $m = 1, \ldots, n+1$. Therefore, we seek to separate the uncertain parameters from the nominal parameters by grouping the uncertain parameters into a structured uncertainty matrix $\Delta = \text{diag}\{\delta\}$ and expressing the system in the $P - \Delta$ control framework shown in figure 1 where $P(s)$ is the generalized transfer function of the system. If the transfer function $P \in \mathbb{R}^{(q_T+n)\times(q_T+3)}$, where q_T is the rank of the uncertainty matrix Δ, is partitioned as

$$P = \begin{bmatrix} P_{11} & P_{12} \\ P_{21} & P_{22} \end{bmatrix} \tag{32}$$

the input–output equations of the generalized transfer function are

$$y_\Delta = P_{11}u_\Delta + P_{12}v_{FB},$$
$$y = P_{21}u_\Delta + P_{22}v_{FB}, \tag{33}$$

where $P_{11} \in \mathbb{R}^{q_T\times q_T}$, $P_{12} \in \mathbb{R}^{q_T\times 3}$, $P_{21} \in \mathbb{R}^{n\times q_T}$, $P_{22} \in \mathbb{R}^{n\times 3}$, $y_\Delta \in \mathbb{R}^{q_T\times 1}$, $u_\Delta \in \mathbb{R}^{q_T\times 1}$, $y \in \mathbb{R}^{n\times 1}$ and $v_{FB} \in \mathbb{R}^{3\times 1}$. The relationship between the system transfer function $G(s)$ and the generalized transfer function $P(s)$ and the uncertainty matrix Δ is expressed as

$$G(s) = P_{22}(s) + P_{21}(s)\Delta\left[I_{q_T} - P_{11}(s)\Delta\right]^{-1}P_{12}(s), \tag{34}$$

where I_{q_T} is a $q_T \times q_T$ identity matrix. See appendix A for a detailed derivation of this model manipulation.

By examining (33), it can be seen that the transfer function P contains information on how both the nominal system and the uncertain parameters affect the output of the system y. The output of the system is driven by the feedback control input v_{FB} and the uncertain input perturbation u_Δ through the transfer functions P_{22} and P_{21}, respectively. The uncertain input perturbation is driven by the uncertain output perturbation y_Δ through the uncertain matrix Δ. Finally, the output perturbation is driven by the feedback control input v_{FB} and the uncertain input perturbation u_Δ through the transfer functions P_{12} and P_{11}, respectively. If there were no uncertain perturbations, i.e. $\Delta = 0$, the input–output equation of the system would be reduced to

$$y = P_{22}v_{FB}. \tag{35}$$

Therefore, the transfer function P_{22} describes the nominal response of the system, and the transfer functions P_{11}, P_{12} and P_{21} describe how the uncertain parameters affect the output of the system.

5.2. Identification and decoupling of relevant control channels

It is desired that the controlled output $y(t)$ be able to track a reference value $r(t)$, therefore, we define the tracking error $e(t)$ as

$$e(t) = r(t) - y(t). \tag{36}$$

The conditions to bring the tracking error exactly to zero are typically not met because the number of controlled outputs (n) is larger than the number of controlled inputs (3). As a result, we can only independently control 3 linear combinations of the output of the system. Therefore, in order to synthesize an effective feedback controller, it is necessary to determine which output directions are the most controllable and which input directions are the most influential. If these directions are not identified, the feedback controller could actuate in a direction that the system does not respond to and a lot of control energy could be spent for a marginal improvement in the value

of the tracking error. The technique we employ to identify and decouple the most relevant control channels is based on a singular value decomposition of the static (steady-state) gain matrix of the nominal state-space system A_0, B_0, C_0 and D_0. The relationship between the outputs y and the inputs v_{FB} of the nominal system is expressed in terms of the nominal transfer function $G_0(s)$ which is defined as

$$G_0(s) = C_0(sI_n - A_0)^{-1}B_0 + D_0 \qquad y = G_0(s)v_{\mathrm{FB}}. \quad (37)$$

To begin the process of determining the relevant control channels, we consider a steady-state performance index $\bar{J}$, which is defined as

$$\bar{J} = \lim_{t\to\infty} e^{\mathrm{T}}(t)Qe(t) = \bar{e}^{\mathrm{T}}Q\bar{e}, \quad (38)$$

where $\bar{e}$ denotes the steady-state tracking error, $(\cdot)^{\mathrm{T}}$ denotes the matrix transpose, and $Q \in \mathbb{R}^{n\times n}$ is a symmetric positive definite matrix that is used to weight which components of the tracking error, relative to the other components, are more important to minimize. Assuming a constant reference $\bar{r}$ and provided the closed-loop system is internally stable, the system can be maintained at steady state, which means the output and the input of the system will reach constant values that define an equilibrium of the closed-loop system. Under these assumptions, the input–output relation in steady state is expressed as

$$\bar{y} = \bar{G}_0\bar{v}_{\mathrm{FB}} = \left(-C_0(A_0)^{-1}B_0 + D_0\right)\bar{v}_{\mathrm{FB}}, \quad (39)$$

where $\bar{y}$ denotes the steady-state output, $\bar{v}_{\mathrm{FB}}$ denotes the steady-state input, and $\bar{G}_0$ denotes the steady-state gain of the plant $G_0(s)$ (i.e. $s \to 0$). We introduce another positive definite matrix $R \in \mathbb{R}^{3\times3}$ to weight which inputs have more control authority relative to the other inputs. We then define the 'weighted' steady-state transfer function $\tilde{G}_0$ and its 'economy' size singular value decomposition [20] as

$$\tilde{G}_0 = Q^{\eta}\bar{G}_0R^{-\eta} = U\Sigma V^{\mathrm{T}}, \quad (40)$$

where $\Sigma = \mathrm{diag}\{\sigma_1, \sigma_2, \sigma_3\} \in \mathbb{R}^{3\times3}$ is a diagonal matrix of steady-state singular values with $\sigma_1 > \sigma_2 > \sigma_3 > 0$, $U \in \mathbb{R}^{n\times3}$ and $V \in \mathbb{R}^{3\times3}$ are matrices that possess the following properties:

$$V^{\mathrm{T}}V = VV^{\mathrm{T}} = I \qquad U^{\mathrm{T}}U = I, \quad (41)$$

where I is an identity matrix with the appropriate dimensions, and $\eta = 1/2$ is chosen to enable the performance index (38) to be written as a function of Σ as will be shown below. The weight matrices Q and R are iteratively chosen based on simulation testing and on a sensitivity analysis of the static gain matrix of the nominal model $\bar{G}_0$.

By employing (40), the steady-state input–output relation (39) is expressed as

$$\bar{y} = Q^{-1/2}\tilde{G}_0R^{1/2}\bar{v}_{\mathrm{FB}} = Q^{-1/2}U\Sigma V^{\mathrm{T}}R^{1/2}\bar{v}_{\mathrm{FB}}. \quad (42)$$

We note that the columns of the matrix $Q^{-1/2}U\Sigma$ define a basis for the subspace of obtainable steady-state output values. Therefore, any obtainable steady-state output can be written as a linear combination $\bar{y}^* \in \mathbb{R}^{3\times1}$ of the basis vectors, and we can write

$$\bar{y} = Q^{-1/2}U\Sigma\bar{y}^* \Longleftrightarrow \bar{y}^* = \Sigma^{-1}U^{\mathrm{T}}Q^{1/2}\bar{y}. \quad (43)$$

This implies that only the component of the reference vector $\bar{r}$ that lies in this subspace will be able to be tracked in steady state. Therefore, we decompose the reference vector as $\bar{r} = \bar{r}_{\mathrm{t}} + \bar{r}_{\mathrm{nt}}$ where $\bar{r}_{\mathrm{t}}$ is the trackable component and $\bar{r}_{\mathrm{nt}}$ is the non-trackable component. The trackable component lies in the subspace, therefore, it can be written as a linear combination $\bar{r}^* \in \mathbb{R}^{3\times1}$ of the basis vectors, and we can write

$$\bar{r}_{\mathrm{t}} = Q^{-1/2}U\Sigma\bar{r}^*. \quad (44)$$

The non-trackable component does not lie in the subspace, therefore it can be expressed as

$$\Sigma^{-1}U^{\mathrm{T}}Q^{1/2}\bar{r}_{\mathrm{nt}} = 0 \Longleftrightarrow \bar{r}^* = \Sigma^{-1}U^{\mathrm{T}}Q^{1/2}(\bar{r}_{\mathrm{t}} + \bar{r}_{\mathrm{nt}}). \quad (45)$$

By defining

$$\bar{v}^*_{\mathrm{FB}} = V^{\mathrm{T}}R^{1/2}\bar{v}_{\mathrm{FB}} \Longleftrightarrow \bar{v}_{\mathrm{FB}} = R^{-1/2}V\bar{v}^*_{\mathrm{FB}}, \quad (46)$$

where $\bar{v}^*_{\mathrm{FB}} \in \mathbb{R}^{3\times1}$, and by employing (43) and (42), a decoupled relationship between the outputs $\bar{y}^*$ and the inputs $\bar{v}^*_{\mathrm{FB}}$ is obtained as

$$\begin{aligned}\bar{y}^* &= \Sigma^{-1}U^{\mathrm{T}}Q^{1/2}\bar{y}\\ &= \Sigma^{-1}U^{\mathrm{T}}Q^{1/2}Q^{-1/2}U\Sigma V^{\mathrm{T}}R^{1/2}\bar{v}_{\mathrm{FB}} = \bar{v}^*_{\mathrm{FB}}.\end{aligned} \quad (47)$$

The steady-state tracking error is now written as

$$\bar{e} = \bar{r} - \bar{y} = Q^{-1/2}U\Sigma(\bar{r}^* - \bar{y}^*) \quad (48)$$

and the performance index (38) is expressed as

$$\begin{aligned}\bar{J} &= \bar{e}^{\mathrm{T}}Q\bar{e} = \left(\bar{r}^* - \bar{y}^*\right)^{\mathrm{T}}\Sigma U^{\mathrm{T}}Q^{-1/2}QQ^{-1/2}U\Sigma\left(\bar{r}^* - \bar{y}^*\right)\\ &= \left(\bar{r}^* - \bar{y}^*\right)^{\mathrm{T}}\Sigma^2\left(\bar{r}^* - \bar{y}^*\right) = \left(\bar{e}^*\right)^{\mathrm{T}}\Sigma^2\left(\bar{e}^*\right) = \sum_{i=1}^{3}\sigma_i^2\left(\bar{e}^*_i\right)^2,\end{aligned} \quad (49)$$

where $\bar{e}^* = \bar{r}^* - \bar{y}^*$, σ_i denotes the ith singular value and $\bar{e}^*_i$ denotes the ith component of $\bar{e}^*$.

We note that the ith singular value acts as a weight parameter for the ith component of the tracking error in (49). It is possible that two sequential singular values could exhibit a large difference in magnitude, i.e. $\sigma_i \gg \sigma_{i+1}$. Therefore, no matter how large the component of the tracking error associated with σ_{i+1} is, its contribution to the overall value of performance index will be small compared to the component of the tracking error associated with σ_i. As a result, if we take all of the singular values into account, we could spend a lot of control effort for only a small improvement in the value of the performance index (49). To avoid this penalty, we partition the singular values into k significant singular values Σ_{s} and $3-k$ negligible singular values Σ_{ns}, and a reduced form of the performance index (49) is written as

$$\bar{J}_s = \left(\bar{r}^*_{\mathrm{s}} - \bar{y}^*_{\mathrm{s}}\right)^{\mathrm{T}}\Sigma^2_{\mathrm{s}}\left(\bar{r}^*_{\mathrm{s}} - \bar{y}^*_{\mathrm{s}}\right) = \left(\bar{e}^*_{\mathrm{s}}\right)^{\mathrm{T}}\Sigma^2_{\mathrm{s}}\left(\bar{e}^*_{\mathrm{s}}\right), \quad (50)$$

where $\bar{e}^*_{\mathrm{s}} \in \mathbb{R}^{k\times1}$ is the significant component of the tracking error, $\bar{r}^*_{\mathrm{s}} = \Sigma^{-1}_{\mathrm{s}}U^{\mathrm{T}}_{\mathrm{s}}Q^{1/2}(\bar{r}_{\mathrm{t}} + \bar{r}_{\mathrm{nt}}) \in \mathbb{R}^{k\times1}$,

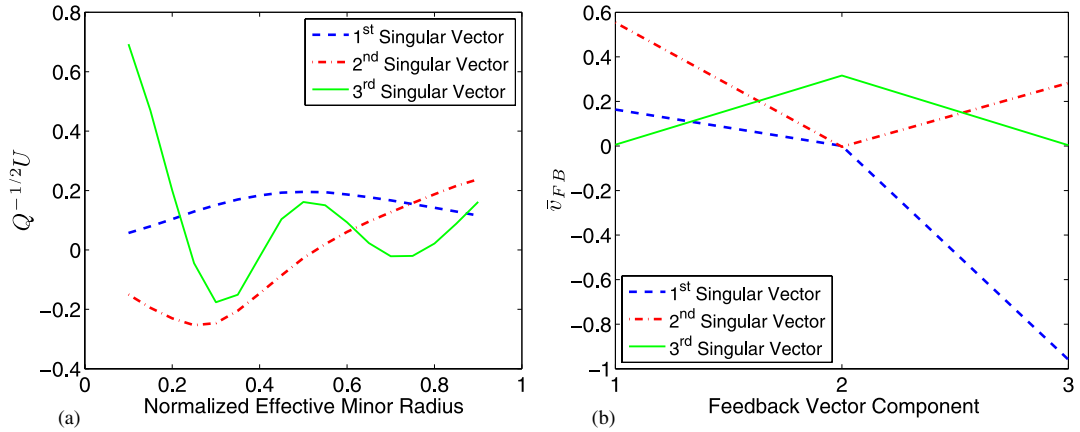

Figure 2. Steady-state (*a*) reference output singular vectors and (*b*) input singular vectors.

$\bar{y}_s^* = \Sigma_s^{-1} U_s^T Q^{1/2} \bar{y} \in \mathbb{R}^{k\times 1}$ and $U_s \in \mathbb{R}^{n\times k}$ and $V_s \in \mathbb{R}^{3\times k}$ are the components of U and V that are associated with the significant singular values. By examining (46), we observe that the significant component of the control input can be defined as $\bar{v}_{FB_s}^* = V_s^T R^{1/2} \bar{v}_{FB} \in \mathbb{R}^{k\times 1}$. See appendix B for a derivation of the reduced performance index and of a reduced form of the decoupled system (47).

The singular vectors of the basis for the subspace of obtainable steady-state output values, and therefore the trackable components of the reference vector, $Q^{-1/2}U$ are shown in figure 2(*a*). The corresponding singular vectors associated with the steady-state input values $R^{-1/2}V$ are shown in figure 2(*b*). The associated singular values are $\sigma_1 = 7.9360$, $\sigma_2 = 0.2738$ and $\sigma_3 = 0.0015$, which are the result of the dynamic model assumptions, the actuator configuration, and the input scaling. As evidenced by the magnitude of the first singular value relative to the others, the first output singular vector is the dominant shape of an achievable steady-state profile, according to the model. In order to generate this profile shape, the feedback controller can actuate in the direction associated with the first input singular vector, which contains a strong contribution from the boundary feedback control component $v_{3_{FB}}$. As the value of the singular value decreases, a larger amount of control effort is needed along the direction of the associated input singular vector to produce a significant contribution to the steady-state profile in the direction of the associated output singular vector.

5.3. Feedback controller synthesis

The control goal is to design a feedback controller that can minimize (1) while using as little feedback control effort as possible and achieve a set of specified closed-loop performance objectives by controlling the significant portion of the output of the system (33). The feedback controller must also be able to stabilize the system for all allowable perturbations Δ. If the controller achieves this goal it is said to robustly stabilize the system. This control problem is shown schematically in figure 3. The blocks $\Sigma_s^{-1} U_s^T Q^{1/2}$ and $R^{-1/2} V_s$ are used to obtain a one-to-one relationship between the outputs and the inputs of the system, which provides us the ability to synthesize a square feedback controller K. The block $\Sigma_s^{-1} U_s^T Q^{1/2}$ extracts the significant component of the tracking error e_s^*

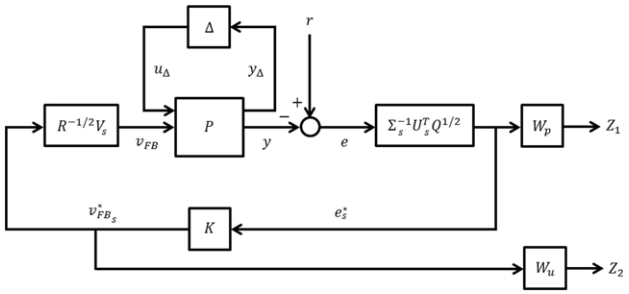

Figure 3. Schematic of control problem formulation.

from the error signal e. The feedback controller is driven by the error e_s^* and outputs the significant component of the feedback control input $v_{FB_s}^*$. Finally, the block $R^{-1/2}V_s$ is used to compute the feedback control input v_{FB} that is applied to the system from the control signal $v_{FB_s}^*$. The outputs of the closed-loop system Z_1 and Z_2 are defined as $Z_1 = W_p e_s^*$ and $Z_2 = W_u v_{FB_s}^*$, where W_p and W_u are frequency dependent functions that will be used to optimize the closed-loop performance of the system during the controller design process by minimizing the frequency-weighted tracking error (Z_1) and control effort (Z_2).

One possible approach to designing a feedback controller K is to directly take the uncertainty Δ into account during the design process. This technique aims to synthesize a feedback controller that robustly stabilizes the system by iterating between controller design and robust stability analysis in a systematic sequence of steps. This approach would guarantee that the designed controller would robustly stabilize the system, however, the computational complexity of this design technique is high, and the iterations may not converge to the best solution. Therefore, we adopt a different approach to synthesize a feedback controller. The technique we employ is to design a nominal controller K to achieve the specified control goals for the nominal closed-loop system, i.e. we assume $\Delta = 0$. We then take the uncertainty Δ into account by analyzing the robust stability of the system with this nominal controller. If the controller successfully robustly stabilizes the system, we have achieved all of our control goals. If the controller does not robustly stabilize the system, we must repeat the process of designing a controller for the

nominal system while relaxing the performance objectives of the closed-loop system.

The H_∞ norm of any stable transfer function $F(s)$ represents the maximum gain in any direction at any frequency between the outputs and inputs of $F(s)$ and is expressed mathematically as

$$||F(s)||_\infty = \max_\omega \bar{\sigma}(F(\mathrm{j}\omega)), \tag{51}$$

where $||\cdot||_\infty$ denotes the H_∞ norm and $\bar{\sigma}(F(\mathrm{j}\omega))$ denotes the maximum singular value of the function F at each frequency ω. For single-input-single-output systems, specifications on the shape of the frequency response of the magnitude of the transfer function F, which is denoted as $|F|$, can be captured by an upper bound, $1/|W_\mathrm{f}(s)|$, on the magnitude of F, where $W_\mathrm{f}(s)$ is a weight function. This frequency dependent specification is expressed mathematically as

$$\begin{aligned} &|F(\mathrm{j}\omega)| < 1/|W_\mathrm{f}(\mathrm{j}\omega)|, \quad \forall\omega \\ \Leftrightarrow\ &|W_\mathrm{f}F| < 1, \ \forall\omega \qquad \Leftrightarrow \qquad ||W_\mathrm{f}F||_\infty < 1, \end{aligned} \tag{52}$$

where the last equivalence relationship follows from the definition of the H_∞ norm (51). This method is easily extendable to multi-input–multi-output systems and yields the same H_∞ relationship between the weight function and the transfer function shown in (52).

We begin the controller design process by writing the nominal performance condition of the closed-loop system shown in figure 3 as

$$\begin{bmatrix} Z_1 \\ Z_2 \end{bmatrix} = \begin{bmatrix} W_\mathrm{p} S_{\mathrm{DC_o}} \\ W_\mathrm{u} K S_{\mathrm{DC_o}} \end{bmatrix} \left[r_\mathrm{s}^* \right], \tag{53}$$

where the function $S_{\mathrm{DC_o}} = (I + \Sigma_\mathrm{s}^{-1} U_\mathrm{s}^\mathrm{T} Q^{1/2} P_{22} R^{-1/2} V_\mathrm{s} K)^{-1}$ is the transfer function from the reference signal r_s^* to the error signal e_s^* (i.e. $e_\mathrm{s}^* = S_{\mathrm{DC_o}} r_\mathrm{s}^*$) and the function $K S_{\mathrm{DC_o}}$ is the transfer function from the reference signal r_s^* to the feedback control signal $v_{\mathrm{FB_s}}^*$ (i.e. $v_{\mathrm{FB_s}}^* = K S_{\mathrm{DC_o}} r_\mathrm{s}^*$). See appendix C for a derivation of this nominal performance condition. We want to synthesize a feedback controller that keeps the tracking error small while using as little feedback control effort as possible for any external reference signal. The outputs of the system naturally lie between zero and one in magnitude, and we have scaled our model so the inputs of the system have a magnitude less than or equal to one. Therefore, we can specify the desired frequency response of the closed-loop transfer functions knowing that all of the control signals (references, outputs, inputs, etc.) are less than or equal to one in magnitude. Typically references are low-frequency signals, therefore, for good reference tracking, the magnitude of the transfer function $S_{\mathrm{DC_o}}$ should approach zero at low frequencies. Accordingly, the feedback controller will need to have some control authority at low frequencies to produce good reference tracking. As a result, the magnitude of the transfer function $K S_{\mathrm{DC_o}}$ should be slightly larger than one at low frequencies. In order to prevent amplification of high-frequency noise in the closed-loop system, such as measurement noise, the peak magnitude of the transfer function $S_{\mathrm{DC_o}}$ needs to be suppressed, and the magnitude of $S_{\mathrm{DC_o}}$ should approach a value of one at high frequencies. In addition, the feedback controller should not react to any high-frequency noise, so the magnitude of the transfer function $K S_{\mathrm{DC_o}}$ should be suppressed below one at high frequencies. Finally, the frequency range over which the feedback controller can actuate the system is specified by placing upper and lower limits on the bandwidth of the closed-loop system.

The functions $W_\mathrm{p}(s)$ and $W_\mathrm{u}(s)$ are used to place upper bounds $1/\bar{\sigma}\left(W_\mathrm{p}(\mathrm{j}\omega)\right)$ and $1/\bar{\sigma}\left(W_\mathrm{u}(\mathrm{j}\omega)\right)$ on the shape of the frequency responses of the magnitude of the transfer functions $S_{\mathrm{DC_o}}$ and $K S_{\mathrm{DC_o}}$, respectively. Therefore, the control design problem is formulated as the following stacked H_∞ minimization problem:

$$\min_K \left|\left| \begin{matrix} W_\mathrm{p} S_{\mathrm{DC_o}} \\ W_\mathrm{u} K S_{\mathrm{DC_o}} \end{matrix} \right|\right|_\infty \qquad \forall\omega, \tag{54}$$

where we have made use of the property (52). The weight functions W_p and W_u are parametrized as [21]

$$W_\mathrm{p}(s) = \frac{\left(s/\sqrt{M_\mathrm{p}} + \omega_\mathrm{p}\right)^2}{\left(s + \omega_\mathrm{p}\sqrt{H_\mathrm{p}^*}\right)^2} \quad W_\mathrm{u}(s) = \frac{\left(s/\sqrt{M_\mathrm{u}} + \omega_\mathrm{u}\right)^2}{\left(s + \omega_\mathrm{u}\sqrt{H_\mathrm{u}^*}\right)^2}, \tag{55}$$

where the parameters M_p and M_u are related to the high-frequency behaviour, the parameters H_p^* and H_u^* are related to the low-frequency behaviour, and the parameters ω_p and ω_u are related to the bandwidth of the upper bounds $1/\bar{\sigma}\left(W_\mathrm{p}(\mathrm{j}\omega)\right)$ and $1/\bar{\sigma}\left(W_\mathrm{u}(\mathrm{j}\omega)\right)$, respectively. The design parameters are chosen as $M_\mathrm{p} = 1$, $H_\mathrm{p}^* = 10^{-4.5}$, $\omega_\mathrm{p} = 10^{-0.3}$, $M_\mathrm{u} = 1$, $H_\mathrm{u}^* = 10^{0.1}$ and $\omega_\mathrm{u} = 1$ so the shape of the frequency response of the upper bounds coincides with the desired shape of the frequency response of the closed-loop transfer functions previously described.

If we are able to find a controller K that minimizes the stacked norm of the transfer functions $W_\mathrm{p} S_{\mathrm{DC_o}}$ and $W_\mathrm{u} K S_{\mathrm{DC_o}}$, we will have minimized the effect a change in the reference r_s^* has on the error e_s^* while using as little feedback control effort $v_{\mathrm{FB_s}}^*$ as possible and achieved a desired performance in the response of the nominal closed-loop system to changes in the reference r_s^*. Therefore, by solving the minimization problem (54), we have synthesized a controller that minimizes (1) while using as little control effort as possible and produces a desired closed-loop response of the system. The feedback controller K found by solving (54) is written in state-space form as

$$\begin{aligned} \dot{x}_c &= A_\mathrm{c} x_\mathrm{c} + B_\mathrm{c} e_\mathrm{s}^*, \\ v_{\mathrm{FB_s}}^* &= C_\mathrm{c} x_\mathrm{c} + D_\mathrm{c} e_\mathrm{s}^*, \end{aligned} \tag{56}$$

where the vector $x_\mathrm{c} \in \mathbb{R}^{p\times 1}$ is the internal controller states, $A_\mathrm{c} \in \mathbb{R}^{p\times p}$, $B_\mathrm{c} \in \mathbb{R}^{p\times 1}$, $C_\mathrm{c} \in \mathbb{R}^{1\times p}$ and $D_\mathrm{c} \in \mathbb{R}^{1\times 1}$ are the controller system matrices and p is the number of controller states. For this controller design, the significant singular values are chosen as $\Sigma_\mathrm{s} = \sigma_1$ and the negligible singular values are chosen as $\Sigma_\mathrm{ns} = \mathrm{diag}\{\sigma_2, \sigma_3\}$. By neglecting the second and third singular values, the feedback controller will be able to actuate the system in the direction associated with the first input singular vector shown in figure 2(*b*) to produce the dominate shape of an achievable steady-state profile associated with the first output singular vector shown in figure 2(*a*). The frequency response of the magnitude of the maximum singular value of the upper bounds $1/W_\mathrm{p}$ and $1/W_\mathrm{u}$ along with the achieved transfer functions $S_{\mathrm{DC_o}}$ and $K S_{\mathrm{DC_o}}$ computed with the nominal controller (56) are shown in figure 4. As can be seen from the figure, the frequency response of the magnitude of the closed-loop transfer functions lie below their respective upper bounds,

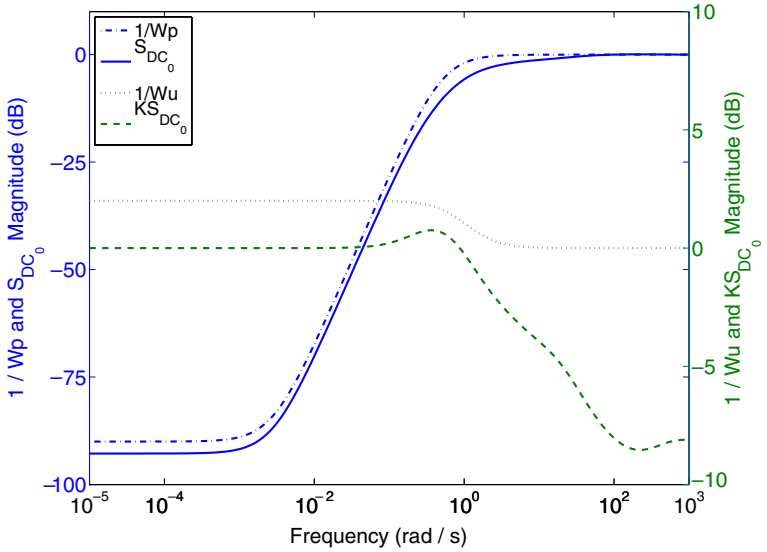

Figure 4. Maximum singular value diagram of: inverse of performance weight $1/W_p$ (dashed–dotted), transfer function S_{DC_o} (solid), inverse of performance weight $1/W_u$ (dot) and transfer function $K S_{DC_o}$ (dash).

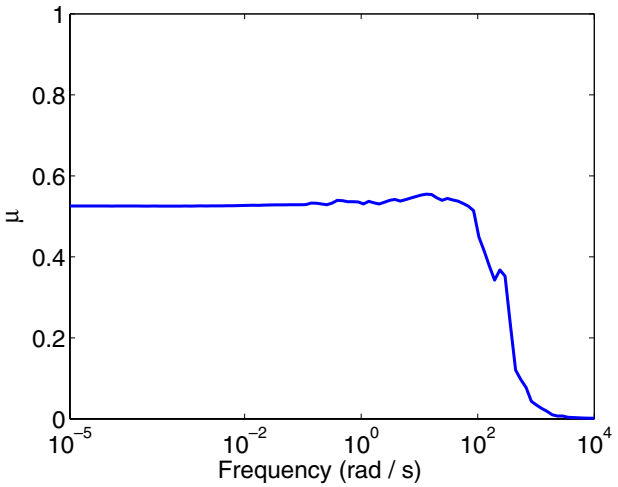

Figure 5. Structured singular value versus frequency.

and the control goals for the nominal closed-loop system are therefore achieved.

We now test the closed-loop system with the nominal controller (56) for robustness against the uncertain perturbations Δ. To analyze the robust stability of the closed-loop system, the structure of the uncertainty is taken into account. Because the uncertainty has a defined structure, $\Delta = \mathrm{diag}\{\delta\}$, we can define the structured singular value μ [21] as

$$\mu\big(N_{11}(\mathrm{j}\omega)\big) = \frac{1}{\min\{k_m \,|\, \det(I - k_m N_{11}\Delta) = 0\}}, \qquad (57)$$

where N_{11} is the transfer function between the signals y_Δ and u_Δ (i.e. $y_\Delta = N_{11}u_\Delta$) in figure 3. See appendix C for a derivation of this transfer function. The closed-loop system is robustly stable for all allowable perturbations if and only if $\mu\big(N_{11}(\mathrm{j}\omega)\big) < 1$, $\forall\omega$ [21]. Figure 5 shows a plot of the achieved structured singular value versus frequency, and as can be seen from the figure, the robust stability condition is satisfied with the nominal controller (56). Therefore, the controller (56) achieves all of our closed-loop control specifications.

The inputs that are applied to the system P are the control signals v_{FB} and the measurements that are available from the system P are the error signals e. Therefore, we must convert the input and output of the controller (56) to these signals. This is accomplished by substituting the relationships $e_s^* = \Sigma_s^{-1} U_s^T Q^{1/2} e$ and $v_{FB} = R^{-1/2} V_s v_{FB_s}^*$ into (56). Finally, the multi-input-multi-output feedback controller $\hat{K} \in \mathbb{R}^{3\times n}$ is expressed in state-space form as

$$\begin{aligned} \dot{x}_c &= A_c x_c + B_c \Sigma_s^{-1} U_s^T Q^{1/2} e, \\ v_{FB} &= R^{-1/2} V_s C_c x_c + R^{-1/2} V_s D_c \Sigma_s^{-1} U_s^T Q^{1/2} e. \end{aligned} \qquad (58)$$

6. Plasma profile control algorithm implementation in the DIII-D PCS

In this section, we describe the implementation of a real-time feedforward + feedback algorithm for magnetic and kinetic profile control in the DIII-D PCS. We provide in section 6.1 an overview of the algorithm implemented in the DIII-D PCS. In section 6.2, we describe the framework for real-time feedforward + feedback control of magnetic and kinetic plasma profiles implemented in the DIII-D PCS. Finally, in section 6.3 we present a simulation simserver that can interface with the DIII-D PCS to test the correctness of the real-time implementation of the control algorithm and to determine the effectiveness of the proposed controller.

6.1. Overview of feedforward + feedback control algorithm

The overall feedforward + feedback control algorithm synthesized from the first-principles-driven model of the poloidal flux profile evolution can be summarized as follows. The feedforward control inputs are computed as

$$u_{1_{FF}}(t) = \left(\frac{\bar{n}_{FF}(t)}{I_{FF}(t)\sqrt{P_{tot_{FF}}(t)}}\right)^{3/2} \qquad u_{2_{FF}}(t) = \frac{\sqrt{P_{tot_{FF}}(t)}}{I_{FF}(t)},$$
$$u_{3_{FF}}(t) = I_{FF}(t), \qquad (59)$$

where $I_{\mathrm{FF}}(t)$, $P_{\mathrm{tot_{FF}}}(t)$ and $\bar{n}_{\mathrm{FF}}(t)$ are determined off-line [15, 16]. In accordance with (17), the feedforward control inputs are modified as

$$v_{1_{\mathrm{FF}}} = u_{1_{\mathrm{FF}}} \qquad v_{2_{\mathrm{FF}}} = u_{2_{\mathrm{FF}}} \qquad v_{3_{\mathrm{FF}}} = u_{1_{\mathrm{FF}}} u_{3_{\mathrm{FF}}}. \tag{60}$$

Finally, the closed-loop control inputs are computed as

$$\begin{aligned} v_1 &= v_{1_{\mathrm{FF}}} + v_{1_{\mathrm{FB}}} u_{1_{\mathrm{norm}}} \qquad v_2 = v_{2_{\mathrm{FF}}} + v_{2_{\mathrm{FB}}} u_{2_{\mathrm{norm}}}, \\ v_3 &= v_{3_{\mathrm{FF}}} + v_{3_{\mathrm{FB}}} u_{1_{\mathrm{norm}}} u_{3_{\mathrm{norm}}}, \end{aligned} \tag{61}$$

where $(\cdot)_{\mathrm{FF}}$ denotes a feedforward quantity and $(\cdot)_{\mathrm{FB}}$ denotes a feedback quantity computed on-line via (58). The closed-loop signals for the control actuators $I(t)$, $P_{\mathrm{tot}}(t)$ and $\bar{n}(t)$ are computed as

$$I(t) = \frac{v_3}{v_1} \qquad P_{\mathrm{tot}}(t) = \left(\frac{v_2 v_3}{v_1}\right)^2 \qquad \bar{n}(t) = \frac{v_2 v_3^2}{v_1^{4/3}}. \tag{62}$$

6.2. *Framework of plasma profile control algorithm in DIII-D PCS*

A general framework for real-time feedforward + feedback control of magnetic and kinetic plasma profiles + a scalar quantity has been implemented in the DIII-D PCS. The magnetic profiles that can be controlled are: the safety factor q, the rotational transform $\iota = 1/q$, the poloidal flux Ψ, or the poloidal flux gradient θ. The kinetic profiles that can be controlled are: the electron temperature, the ion temperature, or the toroidal rotation velocity. The scalar quantities that can be controlled are: the normalized plasma beta β_{N}, the minimum value of q, or the internal inductance of the plasma. The selected magnetic profile can be controlled at 20 evenly spaced points on the domain $\hat{\rho} \in [0.05, 1]$, and the selected kinetic profiles can be controlled at 10 evenly spaced points on the domain $\hat{\rho} \in [0.1, 1]$. The feedback portion of the controller was interfaced with the real-time EFIT (rtEFIT) equilibrium reconstruction code [22] for magnetic profile control and with the real-time charge-exchange recombination (rtCER) code [23] for kinetic profile control. The control scheme in this work has only been designed to control the magnetic poloidal flux gradient profile, therefore, only the magnetic profile portion of the control algorithm implemented in the DIII-D PCS is described below.

The diagnostics provided to the PCS by rtEFIT, are the plasma current I, the poloidal stream function at the magnetic axis ψ_{axis} and at the plasma boundary ψ_{bdry}, and the safety factor q on a normalized flux spatial domain ψ_{n} where

$$\psi_{\mathrm{n}} = \frac{\psi - \psi_{\mathrm{axis}}}{\psi_{\mathrm{bdry}} - \psi_{\mathrm{axis}}}. \tag{63}$$

The safety factor $q(\psi_{\mathrm{n}}^{\mathrm{rt}})$ is provided by rtEFIT at 64 evenly spaced points

$$\psi_{n_k}^{\mathrm{rt}} = 0, 1/64, 2/64, \ldots, 63/64. \tag{64}$$

The feedback portion of the controller was implemented as a discrete time state-space system with a sampling time of 20 ms. This sampling time was set based on the modulation of the MSE beam used to obtain q profile measurements in real-time. In this case the MSE beam was modulated on for 10 ms then off for 10 ms. The configuration between the real-time code running in the DIII-D PCS and the DIII-D tokamak is shown in figure 6. The coordinate transformation block in the PCS is an algorithm that is executed to construct the selected magnetic profile $y_{\mathrm{M}}(\hat{\rho})$, either q, ι, Ψ or θ, controlled by the feedback controller from the data provided by the rtEFIT algorithm $q(\psi_{\mathrm{n}}^{\mathrm{rt}})$, ψ_{axis}, ψ_{bdry} and I. See appendix D for a derivation of this algorithm. By implementing the feedback controller with two input signals, $r_{\mathrm{M}} - y_{\mathrm{M_{FF}}}$ and $y_{\mathrm{M}} - y_{\mathrm{M_{FF}}}$, controllers designed with different tracking error definitions can be employed with the same implementation configuration. The nonlinear transformation block in the PCS represents the conversion (62) of the outputs prescribed by the feedforward + feedback controller to the control signals $I(t)$, $P_{\mathrm{tot}}(t)$ and $\bar{n}(t)$. This PCS configuration provides us the ability to introduce artificial input disturbances through the signal v_{d} in figure 6 and to specify various target profile trajectories through the signal r_{M} in figure 6. These two signals allow us to test the feedback controller in reference tracking and disturbance rejection experiments.

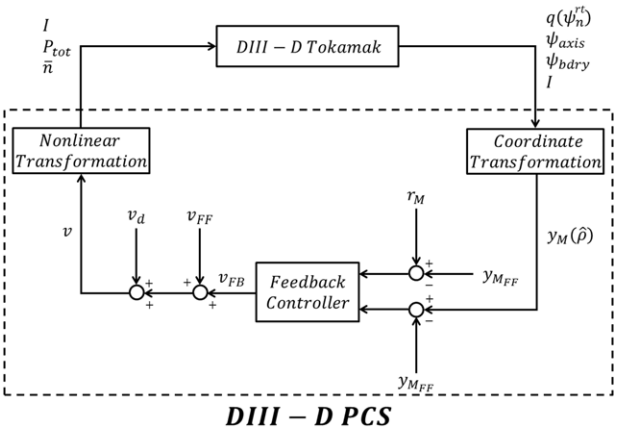

Figure 6. Configuration between the DIII-D tokamak and the DIII-D PCS real-time code for magnetic profile control.

It is important to note that the requests made by the combined feedforward + feedback controller are the references to the respective control loops commanding the physical actuators. For example, in the case of the plasma current, a PID loop regulates the ohmic coil voltage so the plasma current follows the desired waveform requested by the feedforward + feedback algorithm. Similarly to the case of the plasma current, a PID loop regulates gas puffing to make the line average density measured by a CO_2 interferometer follow the combined controller requested density. Finally, the neutral beam control loop manages the individual beam modulation to follow the total average neutral beam power request made by the feedforward + feedback controller. Recent experiments in DIII-D have shown the possibility of controlling both the plasma current and the neutral beam power very accurately. However, the control of the line average density appears more challenging.

We also note that the q profile is not a directly measurable quantity and is reconstructed for feedback control by combining diagnostic measurements with a real-time Grad-Shafranov equilibrium solver, which is the case for the rtEFIT algorithm. However, the accuracy of this reconstruction

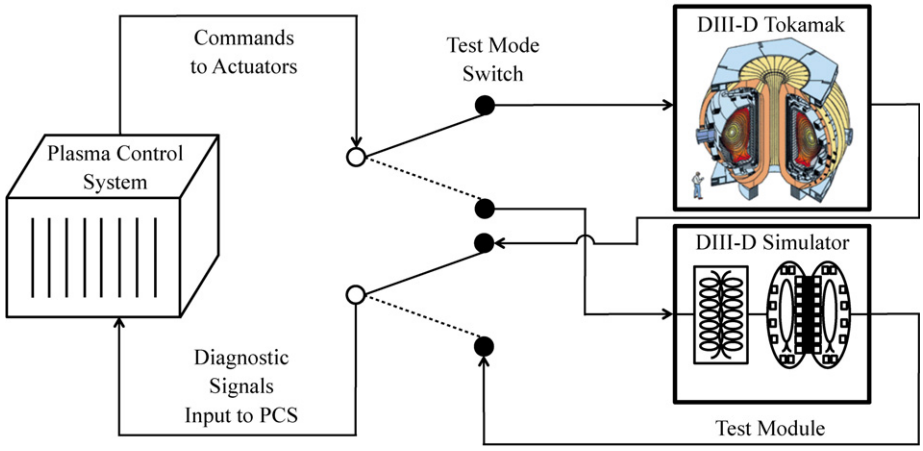

Figure 7. Simserver architecture.

method is limited by the difficulty of obtaining reliable internal plasma diagnostic measurements with adequate spatial and temporal resolution to obtain a complete description of the q profile evolution during the discharge. An alternative approach to constructing the q profile in real-time is to synthesize a closed-loop observer based on the first-principles-driven, physics-based model that governs its evolution, i.e. the same model used to synthesize the feedback controller in this work. The dynamics of the closed-loop observer would filter any diagnostic measurement noise not consistent with the physics of the current profile evolution that propagates through the currently employed reconstruction algorithm, thus providing a more complete picture of the magnetic profile evolution during the plasma discharge.

If the feedfoward + feedback controller drives the physical control actuators to saturation, causing any integral component of the feedback controller to wind up, undesirable oscillations in the system could develop. Therefore, some type of anti-windup design is necessary to ensure that the closed-loop system remains well behaved in the presence of actuator saturation. The approach taken here is to augment the given feedforward + feedback controller (59)–(62) with an anti-windup compensation feedback designed to guarantee stability and keep the feedforward + feedback controller well behaved when actuator saturation is present. This is accomplished through the addition of another input signal to the feedback portion of the combined controller. When there is no actuator saturation, the anti-windup compensator leaves the nominal closed-loop system unmodified. See [24] for an example of the employed anti-windup augmentation.

6.3. Simserver architecture

The simulation simserver (Simserver) architecture is a valuable simulation environment which is used for testing algorithms running in the DIII-D PCS, and its architecture is shown in figure 7. It incorporates a tokamak simulation model that is used to test the PCS in realistic closed-loop simulations. The simulation model accepts control inputs from the PCS and then generates simulated diagnostics. A test switch connects the PCS (left) to either the DIII-D tokamak (upper right) or the DIII-D simulated tokamak (bottom right) depending on which mode of operation is selected. The Matlab/Simulink modelling environment is used to model the major features of the tokamak, and the only restriction on the Simulink models is that their inputs and outputs must be consistent with the input and output channels in the PCS. This type of simulation is used to determine the effectiveness of controllers and correctness of their real-time implementation before experimental tests are conducted [25, 26].

In order to carry out a Simserver simulation, a Simulink model of the magnetic diffusion equation (7) was developed and integrated into a Simserver that can interface with the DIII-D PCS. To construct the model, the governing infinite dimensional PDE (7) is approximated by a finite dimensional system of ODEs. The process used to obtain the reduced-order model is the same one used in section 4 where the non-dimensional spatial domain is represented as l nodes while the time domain is left continuous. This discretization process results in l ordinary differential equations that can be integrated in time to simulate the current profile evolution in response to the control actuator signals. In order to be compatible with the diagnostics provided to the PCS by rtEFIT, the Simulink model of the magnetic diffusion equation is required to output the plasma current $I(t)$, the poloidal stream function at the magnetic axis ψ_{axis} and at the plasma boundary ψ_{bdry}, and the safety factor $q(\psi_{\text{n}}^{\text{rt}})$.

7. Simserver simulation testing of control algorithm

In this section, we show results from a Simserver simulation used to test the implementation of the control algorithm (59)–(62) in the DIII-D PCS and to demonstrate the effectiveness of the proposed control algorithm. In order to test the feedback controller in a realistic tokamak operating scenario we need to generate simulation conditions where there is a mismatch (i) between the actual and the assumed initial conditions and (ii) between the actual plant and the model used for the control design. The nominal initial poloidal flux gradient profile $\theta(\hat{\rho})$ is shown in figure 8, which is extracted from DIII-D shot # 129412 at an experimental time of $t = 0.5$ s. In order to satisfy the first simulation condition requirement, we perturb the initial θ profile as shown in figure 8. We denote as the nominal model the PDE model of the θ profile evolution in a

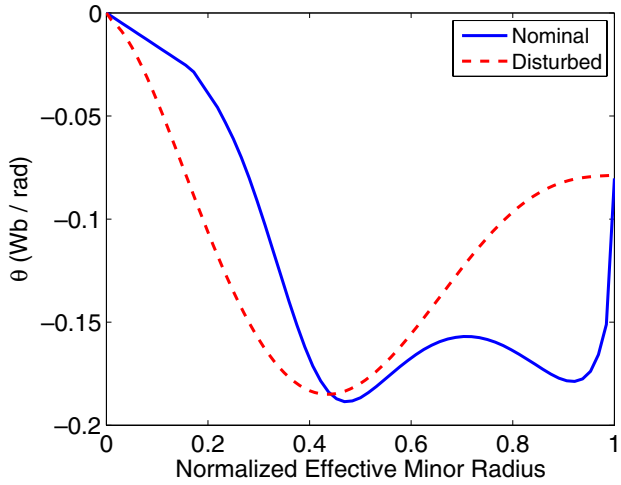

Figure 8. (Simulation reference tracking) Initial poloidal flux gradient profile $\theta(\hat{\rho})$ at time $t = 0.5$ s.

tokamak presented in section 3. This nominal model is used to design both the feedforward and the feedback controllers. In order to satisfy the second simulation condition requirement, we perturb the nominal electron temperature model (4) and non-inductive current density model (5) as

$$T_{\mathrm{e}}^{\mathrm{profile,dis}}(\hat{\rho}) = a \times T_{\mathrm{e}}^{\mathrm{profile}}(\hat{\rho}) \qquad k_{T_{\mathrm{e}}}^{\mathrm{dis}} = a \times k_{T_{\mathrm{e}}},$$
$$j_{\mathrm{NI_{par}}}^{\mathrm{profile,dis}}(\hat{\rho}) = a \times j_{\mathrm{NI_{par}}}^{\mathrm{profile}}(\hat{\rho}) \qquad k_{\mathrm{NI_{par}}}^{\mathrm{dis}} = a \times k_{\mathrm{NI_{par}}}, \tag{65}$$

where $a = 1.1$ in order to produce a plant (disturbed model) that is different from the nominal model used to synthesize the control algorithm. These simulation conditions provide the means to test the feedback controller in a realistic operating scenario where there is a mismatch between the actual and the assumed initial conditions and between the plant and the model.

We now describe the setup for a test conducted to determine the reference tracking capabilities of the feedback controller through simulation with the real-time code utilized in the DIII-D PCS. We begin by producing a target poloidal flux gradient profile evolution $\theta_{\mathrm{tar}}(\hat{\rho}, t)$ by executing a feedfoward control only simulation, i.e. $v_{\mathrm{FB}} = v_{\mathrm{d}} = 0$ in figure 6, with the optimal feedforward control inputs $v_{\mathrm{FF_{Opt}}}$ [15, 16]. For this simulation, the Simserver simulates the nominal model with the nominal initial condition. Next, we produce a second poloidal flux gradient profile evolution $\theta_{\mathrm{FF}}(\hat{\rho}, t)$ that is different from the target evolution $\theta_{\mathrm{tar}}(\hat{\rho}, t)$. This is accomplished by generating a non-optimal set of feedfoward control trajectories v_{FF} by perturbing the optimal feedfoward control inputs and then executing another feedfoward control only simulation with these perturbed control inputs. For this simulation, the Simserver simulates the disturbed model (plant) with the perturbed initial condition. Finally, we determine the ability of the feedback controller to track the target profile evolution $\theta_{\mathrm{tar}}(\hat{\rho}, t)$ by executing a feedforward + feedback control simulation. For this simulation, the Simserver simulates the disturbed model (plant) with the perturbed initial condition. The setup of the feedforward + feedback simulation is as follows. The feedback controller is on for the duration of the simulation, the non-optimal feedforward control inputs v_{FF} are used, no input disturbances are applied, i.e. $v_{\mathrm{d}} = 0$, and the reference vector is set according to $r_{\mathrm{M}}(\hat{\rho}, t) = \theta_{\mathrm{tar}}(\hat{\rho}, t)$. The tracking error e is defined at any time t during the simulation as

$$e = (r_{\mathrm{M}} - y_{\mathrm{M_{FF}}}) - (y_{\mathrm{M}} - y_{\mathrm{M_{FF}}}) = \left[\theta_{\mathrm{tar}}(\hat{\rho}) - \theta_{\mathrm{FF}}(\hat{\rho})\right] - \left[\theta(\hat{\rho}) - \theta_{\mathrm{FF}}(\hat{\rho})\right] = \theta_{\mathrm{tar}}(\hat{\rho}) - \theta(\hat{\rho}), \tag{66}$$

which in turn implies the feedback controller is trying to drive the θ profile to the desired target profile.

The ramp-up phase of the simulated discharges corresponds to an experimental time $t = [0.5, 1.7]$ s, and the early flat-top phase of the simulated discharges is associated with the experimental time $t = [1.7, 2.9]$ s. A comparison between the target profile, the θ profile achieved by the plant (disturbed model) with feedforward + feedback control, and the θ profile achieved by the plant with feedforward only control at experimental times $t = 1.7$, $t = 2.3$ and $t = 2.9$ s is shown in figure 9. During the ramp-up phase, the feedback controller reacts to the initial tracking error and begins to drive the plant towards the target. At the end of the ramp-up phase, the modification of the θ profile of the plant towards the target profile is evident as shown in figure 9(a). As the feedforward + feedback simulation progresses into the beginning of the flat-top phase, the feedback controller is able to successfully drive the plant to the target profile and then regulate the θ profile evolution around the target trajectory as shown in figures 9(b) and 9(c). A comparison of the feedforward and feedforward + feedback control trajectories for $I(t)$, $P_{\mathrm{tot}}(t)$ and $\bar{n}(t)$ is shown in figure 10. In order to (i) track the target profile evolution, (ii) overcome the disturbance in the initial θ profile and (iii) overcome the uncertainty in the plant, the feedback component of the combined controller modifies the non-optimal feedforward control trajectories throughout the feedforward + feedback simulation.

8. Experimental testing of control algorithm

The actuators used to manipulate the poloidal flux gradient profile evolution $\theta(\hat{\rho}, t)$ have a limited ability to drive the system towards a desired target profile based on the physical design of the DIII-D tokamak. As a result, there are a limited number of target profiles that are physically achievable by the machine no matter what type of profile control strategy is employed. The control actuators themselves are also physically constrained in magnitude as well as rate of change, which further reduces the range of target profiles achievable for a given initial θ profile. The goal of the experimental tests was to verify that the feedback controller synthesized from a first-principles-driven model of the poloidal flux profile evolution is able to drive the system to a target profile that is physically achievable by the machine. Towards this goal, we first sought a target poloidal flux gradient profile evolution $\theta_{\mathrm{tar}}(\hat{\rho}, t)$ that was physically achievable by the machine. We executed a feedfoward control only discharge with a nominal set of feedforward control inputs $v_{\mathrm{FF_{Nom}}}$ in DIII-D shot # 145477, and from this discharge we extracted a physically achievable target profile evolution that we employed to test the feedback controller in reference tracking and disturbance rejections experiments.

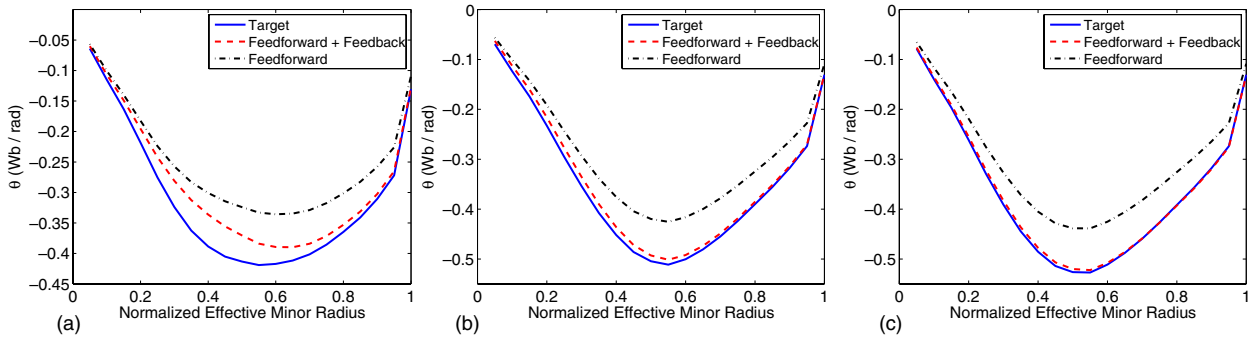

Figure 9. (Simulation reference tracking) Poloidal flux gradient profile $\theta(\hat{\rho})$ at time (*a*) $t = 1.7$ s, (*b*) $t = 2.3$ s and (*c*) $t = 2.9$ s.

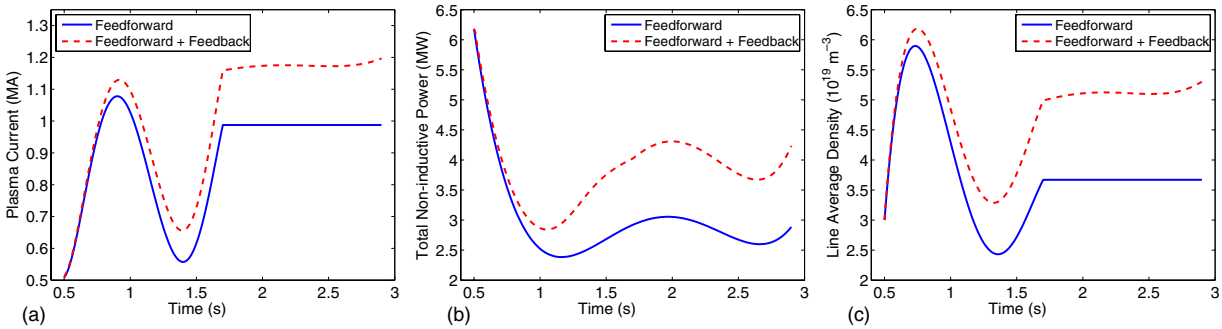

Figure 10. (Simulation reference tracking) Control trajectory comparison: (*a*) plasma current (MA), (*b*) total non-inductive power (MW) and (*c*) line average density (10^{19} m^{-3}).

8.1. Reference tracking

In this subsection we describe the results of a test designed to determine the reference tracking capabilities of the feedback controller in the DIII-D tokamak during the ramp-up and early flat-top phases of the discharge. We first produced a poloidal flux gradient profile evolution $\theta_{\mathrm{FF}}(\hat{\rho}, t)$ that was different from the target evolution $\theta_{\mathrm{tar}}(\hat{\rho}, t)$. This profile evolution was obtained by perturbing the nominal feedfoward control inputs to obtain a second set of feedfoward control inputs $u_{\mathrm{FF_{Ptrb}}}$ and executing a feedfoward control only discharge in DIII-D shot # 146411. Next, we determined the ability of the feedback controller to track the target profile evolution $\theta_{\mathrm{tar}}(\hat{\rho}, t)$ by executing a feedforward + feedback control discharge in DIII-D shot # 146458. During this discharge, the feedback controller was on for the duration of the experiment, the feedforward control inputs $u_{\mathrm{FF_{Ptrb}}}$ were used as the feedforward component of the combined controller, and the reference vector was set according to $r_{\mathrm{M}}(\hat{\rho}, t) = \theta_{\mathrm{tar}}(\hat{\rho}, t)$. As seen in (66), this choice of the reference vector implies the feedback controller was trying to drive the θ profile to the desired target profile.

In the reference tracking experiment, the ramp-up phase was associated with the time $t = [0.5, 1.2]$ s, and the early flat-top phase corresponded to the time $t = [1.2, 2.25]$ s. Time traces of the poloidal flux gradient θ at normalized radii $\hat{\rho} = 0.3$, 0.4, 0.6, 0.7, 0.8 and 0.9 achieved during the target discharge, the feedforward + feedback control discharge and the feedforward control discharge are shown in figure 11. The feedback controller can manipulate the θ profile evolution through diffusivity, interior and boundary actuation. Due to the fact that the boundary actuation is one of the more influential actuators as shown in figure 2(*b*), the feedback controller can more effectively control the θ profile near the plasma boundary because of the spatial proximity of the actuator and the controlled quantity. Therefore, a tracking error in the interior of the plasma will take longer to be eliminated because the control action applied at the plasma boundary will have to diffuse towards the centre of the plasma. This behaviour is shown in figures 11(*c*)–(*f*) for the time traces of θ at normalized radii $\hat{\rho} = 0.6$, 0.7, 0.8 and 0.9 achieved in the feedforward + feedback control discharge. During this discharge, the θ evolution at $\hat{\rho} = 0.6$ and 0.7 was initially below the desired target evolution. Therefore, the feedback controller caused θ at $\hat{\rho} = 0.8$ and 0.9 to overshoot the desired target evolution at these spatial locations in order to cause the θ evolution at $\hat{\rho} = 0.6$ and 0.7 to increase towards the target evolution through diffusion. Once the target θ evolution was achieved at $\hat{\rho} = 0.6$ and 0.7 at the time $t = 2.0$ s as shown in figures 11(*c*) and (*d*), the feedback controller began to reduce the tracking error at the normalized radii $\hat{\rho} = 0.8$ and 0.9 during the time interval $t = [2.0, 2.25]$ s as shown in figures 11(*e*) and (*f*).

A comparison between the target profile, the $\theta(\hat{\rho})$ profile achieved in the feedforward + feedback control discharge, and the $\theta(\hat{\rho})$ profile achieved in the feedforward control discharge at times $t = 0.538$, $t = 1.218$, $t = 1.618$ and $t = 2.258$ s is shown in figure 12. Due to the nonlinear behaviour of the tokamak plasma and the physical limitations of the actuators to manipulate the θ profile evolution, there was no guarantee that the feedback controller would be able to drive the θ profile evolution in the feedforward + feedback control discharge to the target profile evolution from the perturbed initial condition shown in figure 12(*a*). During the ramp-up phase of the feedforward + feedback control discharge, the

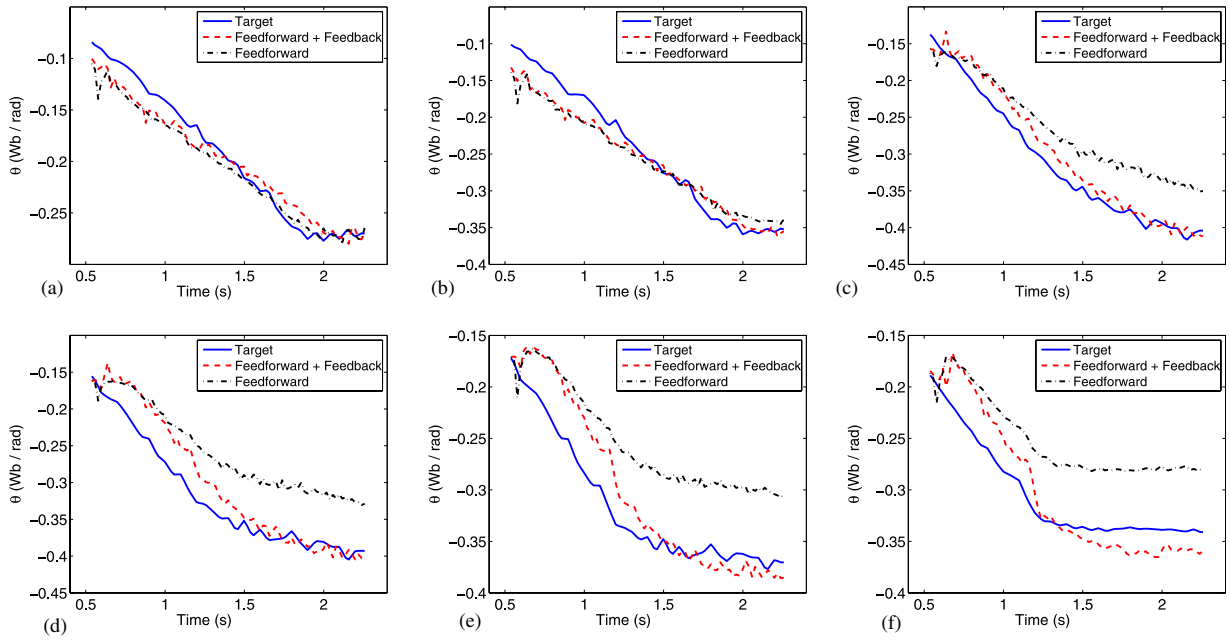

Figure 11. (Experiment reference tracking) Time trace of poloidal flux gradient θ at normalized radii (*a*) $\hat{\rho} = 0.3$, (*b*) $\hat{\rho} = 0.4$, (*c*) $\hat{\rho} = 0.6$, (*d*) $\hat{\rho} = 0.7$, (*e*) $\hat{\rho} = 0.8$ and (*f*) $\hat{\rho} = 0.9$.

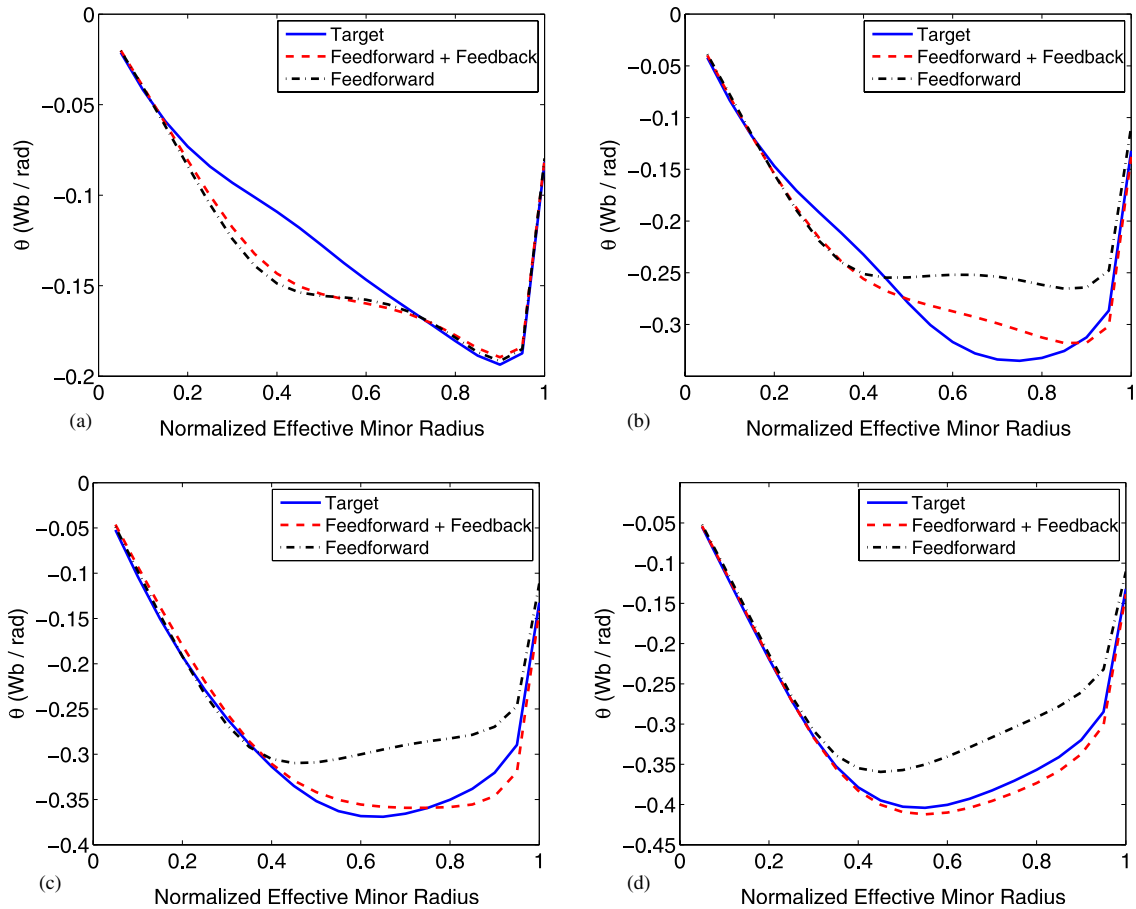

Figure 12. (Experiment reference tracking) Poloidal flux gradient profile $\theta(\hat{\rho})$ at time (*a*) $t = 0.538$ s, (*b*) $t = 1.218$ s, (*c*) $t = 1.618$ s and (*d*) $t = 2.258$ s.

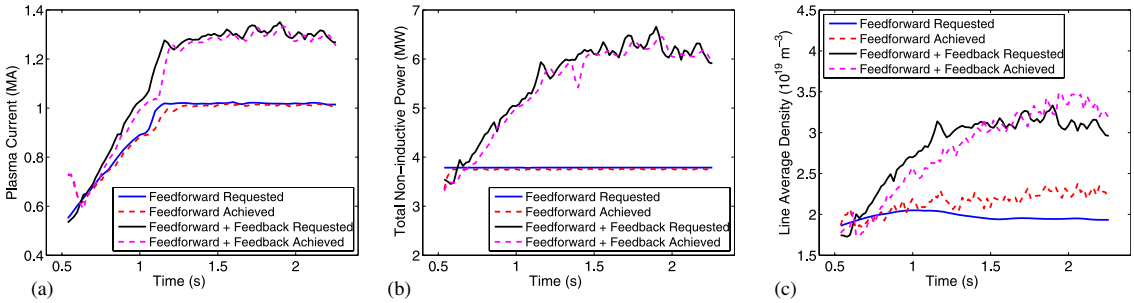

Figure 13. (Experiment reference tracking) Control trajectory comparison: (*a*) plasma current (MA), (*b*) total non-inductive power (MW) and (*c*) line average density (10^{19} m^{-3}).

feedback controller began to drive the plasma towards the target profile by modifying the perturbed feedforward actuator trajectories as shown in figures 12(*b*) and (*c*). At the end of the early flat-top phase of the feedforward + feedback control discharge, the feedback controller was able to drive the θ profile as close as possible to the target profile as shown in figure 12(*d*).

A comparison of the actuator trajectories during the feedforward control discharge and during the feedforward + feedback control discharge is shown in figure 13. In order to track the target profile evolution, the feedback component of the combined controller modified the actuator trajectories throughout the feedforward + feedback control discharge. Also shown in figure 13 is the ability of the control loops commanding the physical actuators to follow the requests made by the control algorithm. The control loops commanding the total plasma current and the total average neutral beam power were able to follow the requests very well, and the control loop commanding the line average density was able to follow the request reasonably well.

8.2. *Disturbance rejection*

In this subsection we describe the results of a test designed to determine the disturbance rejection capabilities of the feedback controller in the DIII-D tokamak during the flat-top phase of the discharge. To determine the ability of the feedback controller to reject an artificial input disturbance, a feedforward + disturbance + feedback control discharge was executed in DIII-D shot # 146153. During this discharge, the nominal feedforward control inputs $v_{\mathrm{FF_{Nom}}}$ were used during the time interval $t = [0.5, 2]$ s (ramp-up and early flat-top phases) with the feedback controller off. During the time interval $t = [2, 5]$ s (flat-top phase), a disturbance was added to the nominal feedforward actuator trajectories. The disturbance was added according to

$$\begin{aligned} v_{1_{\mathrm{FF_{dis}}}} &= u_{1_{\mathrm{FF_{Nom}}}} \qquad v_{2_{\mathrm{FF_{dis}}}} = u_{2_{\mathrm{FF_{Nom}}}}, \\ v_{3_{\mathrm{FF_{dis}}}} &= u_{1_{\mathrm{FF_{Nom}}}}\left[u_{3_{\mathrm{FF_{Nom}}}} - 0.1\right] \end{aligned} \tag{67}$$

to produce a feedforward + disturbance set of control inputs $v_{\mathrm{FF_{dis}}}$. By examining (62) it can be seen that this disturbance will propagate into each of the three control actuators $I(t)$, $P_{\mathrm{tot}}(t)$ and $\bar{n}(t)$. The feedback controller was turned on and off throughout this discharge according to

$$v_{\mathrm{FB}} = \begin{cases} 0.5 \text{ to } 2.2\,\mathrm{s} & \mathrm{OFF} \\ 2.2 \text{ to } 2.7\,\mathrm{s} & \mathrm{ON} \\ 2.7 \text{ to } 3.2\,\mathrm{s} & \mathrm{OFF} \\ 3.2 \text{ to } 5.0\,\mathrm{s} & \mathrm{ON} \end{cases} \tag{68}$$

to see the effect the disturbance had on the plasma and to determine the ability of the feedback controller to reject the disturbance and regulate the θ profile evolution around the target profile evolution. The reference vector was set according to $r_{\mathrm{M}}(\hat{\rho}, t) = \theta_{\mathrm{tar}}(\hat{\rho}, t)$, which implies the feedback controller was trying to regulate the θ profile around the desired target profile.

A comparison between the target profile and the $\theta(\hat{\rho})$ profile achieved during DIII-D shot # 146153 (FF + Dist. + FB) at several times throughout the discharge is shown in figure 14. When the disturbance was initially introduced to the plasma at the time $t = 2.0$ s, the θ profile was close to the desired target profile as shown in figure 14(*a*). During the time interval $t = [2.0, 2.2]$ s, the disturbance slightly moved the θ profile away from the target profile as shown in figure 14(*b*). At the time $t = 2.2$ s, the feedback controller was turned on and it was able to reject the effects of the disturbance. This resulted in the target profile being successfully achieved when the feedback controller was turned off at the time $t = 2.7$ s as shown in figure 14(*c*). During the time interval $t = [2.7, 3.2]$ s, the θ profile again drifted away from the target profile due to the disturbance as shown in figure 14(*d*). Finally, the feedback controller was turned on for the remainder of the discharge at the time $t = 3.2$ s and it was once again able to reject the effects the disturbance had on the θ profile evolution. This resulted in the θ profile evolution being driven to and then successfully regulated around the target profile evolution as shown in figures 14(*e*) and (*f*).

Time traces of θ at normalized radii $\hat{\rho} = 0.3$, 0.4, 0.6, 0.7, 0.8 and 0.9 achieved during the target discharge and DIII-D shot # 146153 are shown in figure 15. The effect the uncontrolled disturbance had on the θ profile evolution can be seen in the time traces of θ at normalized radii $\hat{\rho} = 0.6$, 0.7, 0.8 and 0.9 as shown in figures 15(*c*)–(*f*). During the time intervals $t = [2.0, 2.2]$ s and $t = [2.7, 3.2]$ s when the feedback controller was off, the disturbance caused θ to drift away from the target. Also shown in these time traces of θ is the ability of the feedback controller to reject the effects of the disturbance and regulate θ around the target during the time intervals $t = [2.2, 2.7]$ s and $t = [3.2, 5.0]$ s when the feedback controller was on.

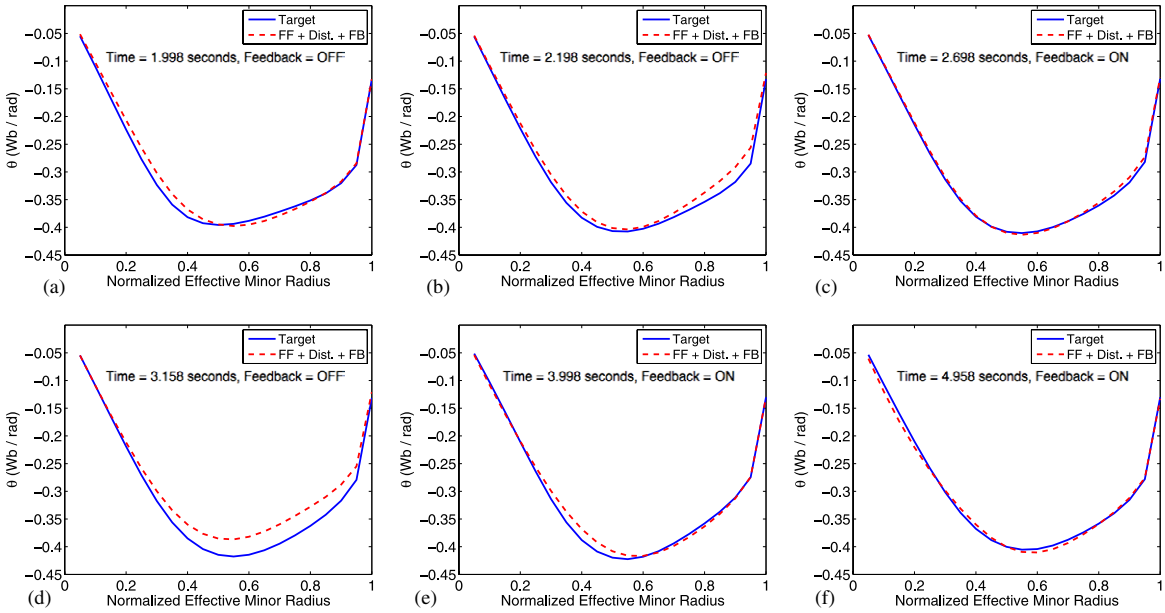

Figure 14. (Experiment disturbance rejection) Poloidal flux gradient profile $\theta(\hat{\rho})$ at time (*a*) $t = 1.998$ s, (*b*) $t = 2.198$ s, (*c*) $t = 2.698$ s, (*d*) $t = 3.158$ s, (*e*) $t = 3.998$ s and (*f*) $t = 4.958$ s.

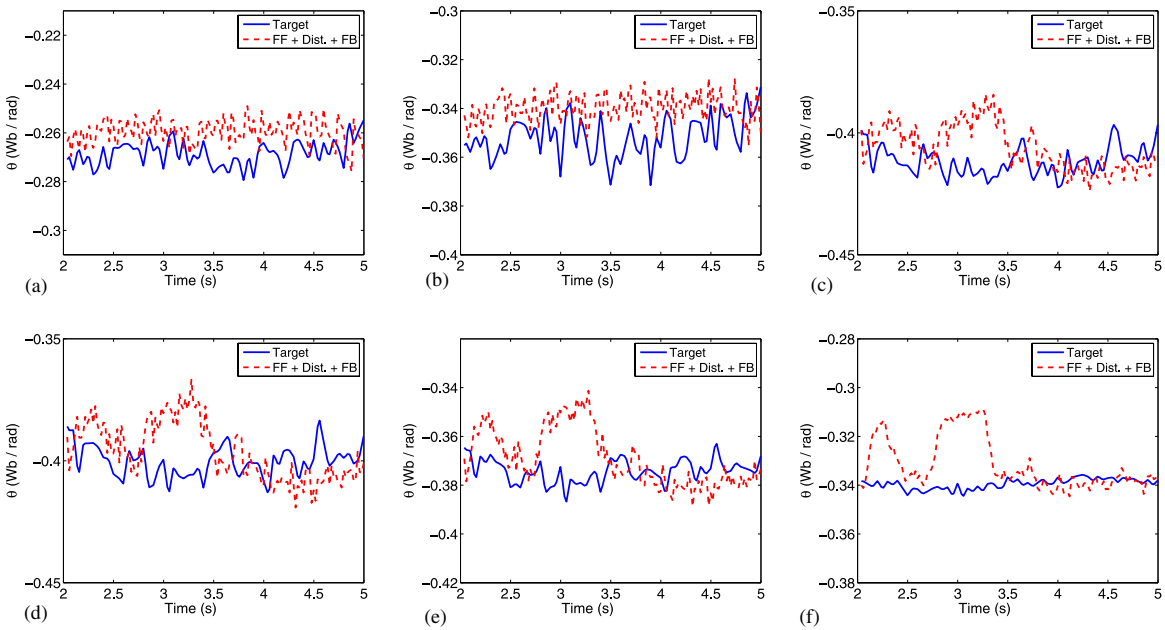

Figure 15. (Experiment disturbance rejection) Time trace of poloidal flux gradient θ at normalized radii (*a*) $\hat{\rho} = 0.3$, (*b*) $\hat{\rho} = 0.4$, (*c*) $\hat{\rho} = 0.6$, (*d*) $\hat{\rho} = 0.7$, (*e*) $\hat{\rho} = 0.8$ and (*f*) $\hat{\rho} = 0.9$.

A comparison of the actuator trajectories during the target discharge and during the feedforward + disturbance + feedback control discharge is shown in figure 16. In order to regulate the θ profile around the target profile and reject the effects of the disturbance, the feedback component of the combined controller modified the actuator trajectories throughout the discharge. The actuator limits during this control test were

$$\begin{aligned} 0.3\,\text{MA} \leqslant I(t) \leqslant 1.5\,\text{MA}, \\ 2.24\,\text{MW} \leqslant P_{\text{tot}}(t) \leqslant 4.4275\,\text{MW}, \\ 2(10)^{19}\,\text{m}^{-3} \leqslant \bar{n}(t) \leqslant 10(10)^{19}\,\text{m}^{-3}. \end{aligned} \tag{69}$$

As can be seen in figure 16, the combined control algorithm drove the line average density request to saturation, however, the line average density requested by the control algorithm was around $1.9(10)^{19}\,\text{m}^{-3}$. Therefore, the level of actuator saturation was small, and the anti-windup compensator was able to successfully keep the closed-loop system well behaved in the presence of the actuator saturation. Also shown in figure 16 is the ability of the control loops commanding the physical actuators to follow the requests made by the combined control algorithm. The control loops commanding the total plasma current and the total average neutral beam power were

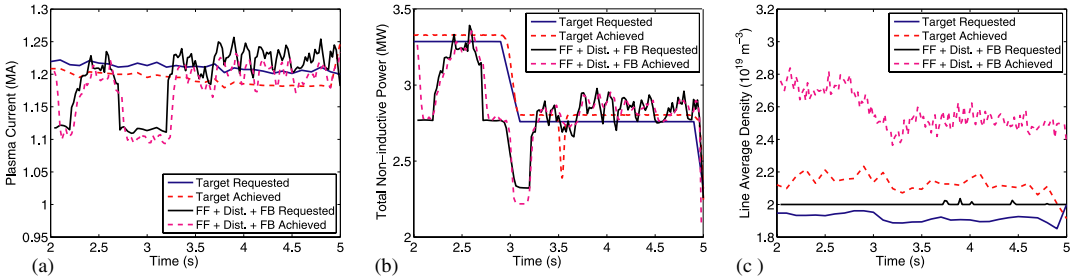

Figure 16. (Experiment disturbance rejection) Control trajectory comparison: (*a*) plasma current (MA), (*b*) total non-inductive power (MW) and (*c*) line average density (10^{19} m^{-3}).

able to follow the requests very well, but the control loop commanding the line average density was not able to follow the request very well. This resulted in an additional, unintentional disturbance the feedback controller needed to overcome.

9. Conclusions and future work

A robust feedback controller was synthesized to control the poloidal flux gradient profile evolution in the DIII-D tokamak from a first-principles-driven model of the poloidal flux profile evolution. A general framework for real-time feedforward + feedback control of magnetic and kinetic plasma profiles was successfully implemented in the DIII-D PCS. The feedback component of the control algorithm was interfaced with the available real-time measurements and successfully tested experimentally during both the ramp-up and flat-top phases of L-mode discharges. Even though the model used to synthesize the feedback controller neglected the effects of the bootstrap current, the adequate performance of the feedback controller during the flat-top phase of the discharge can be attributed to the facts that the effects of the bootstrap current on the θ profile evolution are typically small in L-mode plasmas and the feedback controller is robust against the unmodelled bootstrap current dynamics in this operating regime. These experiments mark the first time ever a first-principles-driven, model-based, closed-loop magnetic profile controller was successfully implemented and tested in a tokamak device.

Now that the performance of the synthesized feedback controller for plasma magnetic profile control has been experimentally validated in L-mode, the combined feedforward + feedback control scheme will be extended to H-mode advanced tokamak operating scenarios. Work towards developing a simplified nonlinear, dynamic, control-oriented PDE model of the poloidal flux profile evolution valid for H-mode plasma discharges will be carried out by once again proposing simplified models for the electron temperature, the plasma resistivity, and the non-inductive current drive. The fact that the characteristic thermal diffusion time is much faster than the characteristic resistive diffusion time will be exploited to determine some of these models. The co-injection neutral beams, the counter-injection neutral beams, and the electron cyclotron heating will be modelled individually rather than together, which may improve the controllability of the current profile by providing additional actuators. The effects of the non-inductive bootstrap current will also be taken into account since they are expected to be significant in H-mode. Finally, first-principles-driven feedforward + feedback control schemes will be proposed to regulate both the magnetic and kinetic plasma profiles around desired target profiles simultaneously in H-mode discharges.

Acknowledgments

This work was supported by the NSF CAREER award program (ECCS-0645086) and the US Department of Energy (DE-FG02-09ER55064, DE-FG02-92ER54141 and DE-FC02-04ER54698).

Appendix A. Representation of time-varying model in robust control framework

By employing (28), the model for the deviation dynamics (27) is expressed as

$$\dot{x}_k = \gamma_v\Big(1+\beta_v\delta_v\Big)\sum_{j=1}^{n}\Gamma_{k,j}x_j + \left[\sum_{i=1}^{n}\Gamma_{k,i}\Big(\gamma_\alpha^i\big(1+\beta_\alpha^i\delta_\alpha^i\big)\Big),\Omega_k,\Pi_k\right]v_{\mathrm{FB}}, \quad \text{(A.1)}$$

where $k = 1, 2, \ldots, n$, x_k denotes the kth component of x, $\Gamma_{k,j}$ denotes the kth row jth column component of Γ, and Ω_k and Π_k denote the kth component of Ω and Π, respectively. This representation of the deviation dynamics is rewritten as

$$\dot{x}_k = \sum_{j=1}^{n}\Big[A_{0_{k,j}} + \delta_v A_{1_{k,j}}\Big]x_j + \Big[B_{0_k} + \sum_{i=1}^{n}\delta_\alpha^i B_{i_k}\Big]v_{\mathrm{FB}}, \quad \text{(A.2)}$$

where

$$A_{0_{k,j}} = \gamma_v\Gamma_{k,j} \qquad A_{1_{k,j}} = \gamma_v\beta_v\Gamma_{k,j},$$
$$B_{0_k} = \left[\sum_{i=1}^{n}\gamma_\alpha^i\Gamma_{k,i},\Omega_k,\Pi_k\right] \qquad B_{i_k} = \big[(\gamma_\alpha^i\beta_\alpha^i)\Gamma_{k,i},0,0\big] \quad \text{(A.3)}$$

and $A_{0_{k,j}}$ and $A_{1_{k,j}}$ denote the kth row jth column component of A_0 and A_1, respectively, and B_{0_k} and B_{i_k} denote the kth component of B_0 and B_i respectively. By defining the total uncertainty vector δ as $\delta = [\delta_\alpha^1, \ldots, \delta_\alpha^n, \delta_v] \in \mathbb{R}^{(n+1)\times 1}$, the representation of the state-space matrices $A(t)$, $B(t)$, C and D given in (29)–(31) is obtained.

A linear system with state-space matrices A, B, C and D has a transfer function representation $G(s) = C(sI_n - A)^{-1}B + D$, where s denotes the Laplace variable and n is the number

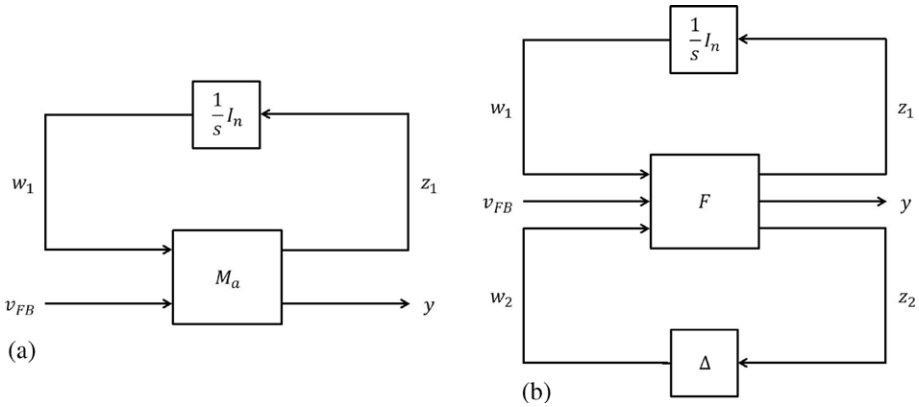

Figure A1. Transfer function $G(s)$ (a) represented as a LFT and (b) with uncertainty Δ pulled out.

of states of the system. By defining the matrix

$$M_a = \begin{bmatrix} A & B \\ C & D \end{bmatrix} \tag{A.4}$$

the system transfer function $G(s)$ can be written as a linear fractional transformation (LFT) as

$$G(s) = D + C(sI_n - A)^{-1}B = D + C\frac{1}{s}I_n\left(I_n - A\frac{1}{s}I_n\right)^{-1}B$$
$$= M_{a_{22}} + M_{a_{21}}\frac{1}{s}I_n\left(I_n - M_{a_{11}}\frac{1}{s}I_n\right)^{-1}M_{a_{12}} = F_{\mathrm{u}}\left(M_a, \frac{1}{s}I_n\right), \tag{A.5}$$

where F_{u} denotes the upper LFT. The block diagram of the system transfer function $G(s)$ (A.5) is shown in figure A1(a) with equivalent equations

$$w_1 = \frac{1}{s}I_n z_1, \quad y = F_{\mathrm{u}}\left(M_a, \frac{1}{s}I_n\right)v_{\mathrm{FB}} = G(s)v_{\mathrm{FB}}. \tag{A.6}$$

By employing (29), the matrix M_a, defined in (A.4), is written in the form of a general affine state-space uncertainty

$$M_a = \begin{bmatrix} A_0 + \sum_{m=1}^{n+1}\delta_m A_m^* & B_0 + \sum_{m=1}^{n+1}\delta_m B_m^* \\ C_0 + \sum_{m=1}^{n+1}\delta_m C_m^* & D_0 + \sum_{m=1}^{n+1}\delta_m D_m^* \end{bmatrix}. \tag{A.7}$$

By exploiting the structure of the state matrices in (A.7), the uncertainty is formulated into a LFT by achieving the smallest possible number of repeated blocks [27]. With this purpose in mind, the matrix J_m is formed as

$$J_m = \begin{bmatrix} A_m^* & B_m^* \\ C_m^* & D_m^* \end{bmatrix} \in \mathbb{R}^{2n\times(n+3)}. \tag{A.8}$$

By using singular value decomposition and grouping terms, the matrix J_m is expressed as

$$J_m = U_m\Sigma_m V_m^* = (U_m\sqrt{\Sigma_m})(\sqrt{\Sigma_m}V_m^*) = \begin{bmatrix} L_m \\ W_m \end{bmatrix}\cdot\begin{bmatrix} R_m \\ Z_m \end{bmatrix}^*, \tag{A.9}$$

where $[\cdot]^*$ denotes the complex conjugate transpose. If the rank of the matrix J_m is q_m, then each inner matrix has the following dimensions:

$$L_m \in \mathbb{R}^{n\times q_m} \quad W_m \in \mathbb{R}^{n\times q_m} \quad R_m \in \mathbb{R}^{n\times q_m} \quad Z_m \in \mathbb{R}^{3\times q_m}. \tag{A.10}$$

By employing (A.9), the uncertainty is written as

$$\delta_m J_m = \begin{bmatrix} L_m \\ W_m \end{bmatrix}[\delta_m I_{q_m}]\begin{bmatrix} R_m \\ Z_m \end{bmatrix}^*, \tag{A.11}$$

where I_{q_m} is a $q_m \times q_m$ identity matrix. Finally the matrix M_a, defined in (A.7), is expressed as

$$M_a = \begin{bmatrix} A_0 & B_0 \\ C_0 & D_0 \end{bmatrix} + \sum_{m=1}^{n+1}\delta_m J_m = F_{11} + F_{12}\Delta F_{21}, \tag{A.12}$$

where

$$F_{11} = \begin{bmatrix} A_0 & B_0 \\ C_0 & D_0 \end{bmatrix} \qquad F_{12} = \begin{bmatrix} L_1 & \dots & L_{n+1} \\ W_1 & \dots & W_{n+1} \end{bmatrix},$$
$$F_{21} = \begin{bmatrix} R_1^* & Z_1^* \\ \vdots & \vdots \\ R_{n+1}^* & Z_{n+1}^* \end{bmatrix} \quad \Delta = \begin{bmatrix} \delta_1 I_{q_1} & & 0 \\ & \ddots & \\ 0 & & \delta_{n+1} I_{q_{n+1}} \end{bmatrix}. \tag{A.13}$$

The representation of the matrix M_a, defined in (A.12), is equal to the lower LFT

$$M_a = F_{\mathrm{l}}(F, \Delta) = F_{11} + F_{12}\Delta(I_{q_{\mathrm{T}}} - F_{22}\Delta)^{-1}F_{21}$$
$$= F_{11} + F_{12}\Delta F_{21}, \tag{A.14}$$

where

$$F = \begin{bmatrix} F_{11} & F_{12} \\ F_{21} & 0 \end{bmatrix} \tag{A.15}$$

q_{T} is the total rank of the Δ matrix given by

$$q_{\mathrm{T}} = \sum_{m=1}^{n+1} q_m \tag{A.16}$$

and F_{l} denotes the lower LFT.

The block diagram of the system is now drawn as in figure A1(b) with equivalent equations

$$w_1 = \frac{1}{s}I_n z_1 \qquad w_2 = \Delta z_2,$$
$$y = F_{\mathrm{u}}\left(F_{\mathrm{l}}(F, \Delta), \frac{1}{s}I_n\right)v_{\mathrm{FB}} = G(s)v_{\mathrm{FB}}. \tag{A.17}$$

The transfer function $G(s)$ of the uncertain state-space model is next expressed as

$$G(s) = F_{\mathrm{u}}\left(M_a, \frac{1}{s}I_n\right) = F_{\mathrm{u}}\left(F_{\mathrm{l}}(F, \Delta), \frac{1}{s}I_n\right)$$
$$= F_{\mathrm{l}}\left(F_{\mathrm{u}}\left(F, \frac{1}{s}I_n\right), \Delta\right) = F_{\mathrm{l}}(P', \Delta). \tag{A.18}$$

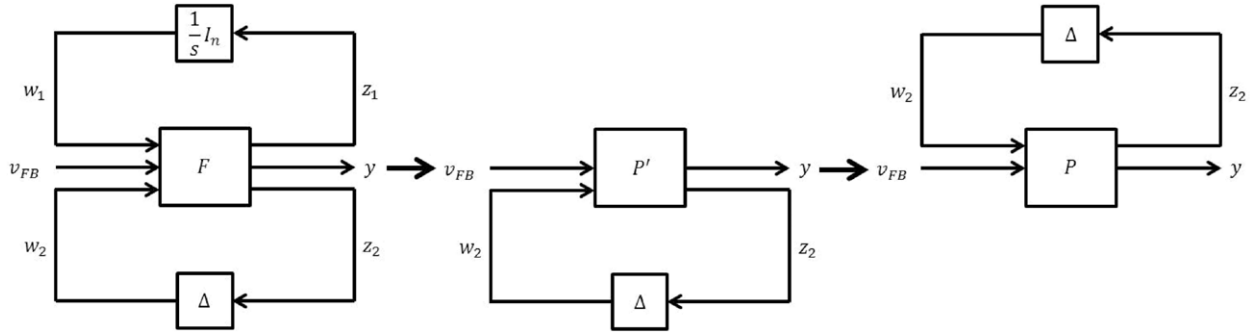

Figure A2. Block diagram manipulation to obtain plant P.

For convention purposes, it is necessary to move the uncertainty to create an upper LFT by employing the definition

$$G(s) = F_l(P', \Delta) = F_u(P, \Delta), \tag{A.19}$$

where

$$P' = \begin{bmatrix} P_{22} & P_{21} \\ P_{12} & P_{11} \end{bmatrix} \qquad P = \begin{bmatrix} P_{11} & P_{12} \\ P_{21} & P_{22} \end{bmatrix}. \tag{A.20}$$

The corresponding block diagram manipulation is shown in figure A2. The input–output equations of the system in this robust control framework are given by (33).

Appendix B. Identification of significant control channels

During the process of determining the relevant control channels, we consider the performance index (49). We partition the singular values into k significant singular values Σ_s and $3-k$ negligible singular values Σ_{ns} and introduce the partitions

$$U = \begin{bmatrix} U_s & U_{ns} \end{bmatrix} \quad V = \begin{bmatrix} V_s & V_{ns} \end{bmatrix} \quad \Sigma = \begin{bmatrix} \Sigma_s & 0 \\ 0 & \Sigma_{ns} \end{bmatrix}, \tag{B.1}$$

$$\bar{r}^* = \begin{bmatrix} \bar{r}_s^* \\ \bar{r}_{ns}^* \end{bmatrix} \qquad \bar{y}^* = \begin{bmatrix} \bar{y}_s^* \\ \bar{y}_{ns}^* \end{bmatrix} \qquad \bar{v}_{FB}^* = \begin{bmatrix} \bar{v}_{FB_s}^* \\ \bar{v}_{FB_{ns}}^* \end{bmatrix}, \tag{B.2}$$

where $U_s \in \mathbb{R}^{n\times k}$, $\Sigma_s \in \mathbb{R}^{k\times k}$, $V_s \in \mathbb{R}^{3\times k}$, $\bar{r}_s^* \in \mathbb{R}^{k\times 1}$, $\bar{y}_s^* \in \mathbb{R}^{k\times 1}$ and $\bar{v}_{FB_s}^* \in \mathbb{R}^{k\times 1}$. By employing the partitions (B.1), the properties $V^T V = I$ and $U^T U = I$ are expressed as

$$V^T V = \begin{bmatrix} V_s^T \\ V_{ns}^T \end{bmatrix} \begin{bmatrix} V_s & V_{ns} \end{bmatrix} = \begin{bmatrix} V_s^T V_s & V_s^T V_{ns} \\ V_{ns}^T V_s & V_{ns}^T V_{ns} \end{bmatrix} = \begin{bmatrix} I & 0 \\ 0 & I \end{bmatrix},$$
$$U^T U = \begin{bmatrix} U_s^T \\ U_{ns}^T \end{bmatrix} \begin{bmatrix} U_s & U_{ns} \end{bmatrix} = \begin{bmatrix} U_s^T U_s & U_s^T U_{ns} \\ U_{ns}^T U_s & U_{ns}^T U_{ns} \end{bmatrix} = \begin{bmatrix} I & 0 \\ 0 & I \end{bmatrix}. \tag{B.3}$$

Using (B.1) and (B.2), we obtain the reduced form of the performance index given by (50). By employing (B.1), (B.3), and using the relationships $\bar{y}_s^* = \Sigma_s^{-1} U_s^T Q^{1/2} \bar{y} \in \mathbb{R}^{k\times 1}$ and $\bar{y} = Q^{-1/2} U \Sigma V^T R^{1/2} \bar{v}_{FB}$, a reduced form of the decoupled system $\bar{y}^* = \bar{v}_{FB}^*$ is expressed as

$$\begin{aligned} \bar{y}_s^* &= \Sigma_s^{-1} U_s^T Q^{1/2} \bar{y} = \Sigma_s^{-1} U_s^T Q^{1/2} Q^{-1/2} U \Sigma V^T R^{1/2} \bar{v}_{FB} \\ &= \Sigma_s^{-1} U_s^T \begin{bmatrix} U_s & U_{ns} \end{bmatrix} \begin{bmatrix} \Sigma_s & 0 \\ 0 & \Sigma_{ns} \end{bmatrix} \begin{bmatrix} V_s^T \\ V_{ns}^T \end{bmatrix} R^{1/2} \bar{v}_{FB} \\ &= \Sigma_s^{-1} \begin{bmatrix} I & 0 \end{bmatrix} \begin{bmatrix} \Sigma_s V_s^T \\ \Sigma_{ns} V_{ns}^T \end{bmatrix} R^{1/2} \bar{v}_{FB} = \bar{v}_{FB_s}^*, \end{aligned} \tag{B.4}$$

where we have defined

$$\bar{v}_{FB_s}^* = V_s^T R^{1/2} \bar{v}_{FB} \Longleftrightarrow \bar{v}_{FB} = R^{-1/2} V_s \bar{v}_{FB_s}^*. \tag{B.5}$$

Appendix C. Derivation of nominal performance condition of closed-loop system

The feedback system shown in figure 3 is expressed in the conventional $\Delta - P^* - K$ robust control design framework shown in figure C1(a) where P^* is the generalized plant, K is the feedback controller, $Z_1 = W_p e_s^*$, $Z_2 = W_u v_{FB_s}^*$ and W_p and W_u are frequency dependent weight functions. The input–output equations of the generalized plant P^* are

$$\begin{bmatrix} y_\Delta \\ Z_1 \\ Z_2 \\ e_s^* \end{bmatrix} = \begin{bmatrix} P_{11}^* & P_{12}^* & P_{13}^* \\ P_{21}^* & P_{22}^* & P_{23}^* \\ P_{31}^* & P_{32}^* & P_{33}^* \\ P_{41}^* & P_{42}^* & P_{43}^* \end{bmatrix} \begin{bmatrix} u_\Delta \\ r_s^* \\ v_{FB_s}^* \end{bmatrix}, \tag{C.1}$$

where

$$\begin{aligned} &P_{11}^* = P_{11} \quad P_{21}^* = -W_p \Sigma_s^{-1} U_s^T Q^{1/2} P_{21} \quad P_{31}^* = 0, \\ &P_{12}^* = 0 \quad P_{22}^* = W_p \quad P_{32}^* = 0, \\ &P_{13}^* = P_{12} R^{-1/2} V_s \quad P_{23}^* = -W_p \Sigma_s^{-1} U_s^T Q^{1/2} P_{22} R^{-1/2} V_s \\ &P_{33}^* = W_u, \quad P_{41}^* = -\Sigma_s^{-1} U_s^T Q^{1/2} P_{21} \quad P_{42}^* = I, \\ &P_{43}^* = -\Sigma_s^{-1} U_s^T Q^{1/2} P_{22} R^{-1/2} V_s. \end{aligned} \tag{C.2}$$

If the generalized plant P^* is partitioned as

$$P^* = \begin{bmatrix} \tilde{P}_{11}^* & \tilde{P}_{12}^* \\ \tilde{P}_{21}^* & \tilde{P}_{22}^* \end{bmatrix}, \tag{C.3}$$

where

$$\begin{aligned} \tilde{P}_{11}^* &= \begin{bmatrix} P_{11}^* & P_{12}^* \\ P_{21}^* & P_{22}^* \\ P_{31}^* & P_{32}^* \end{bmatrix} \qquad \tilde{P}_{12}^* = \begin{bmatrix} P_{13}^* \\ P_{23}^* \\ P_{33}^* \end{bmatrix}, \\ \tilde{P}_{21}^* &= \begin{bmatrix} P_{41}^* & P_{42}^* \end{bmatrix} \qquad \tilde{P}_{22}^* = \begin{bmatrix} P_{43}^* \end{bmatrix} \end{aligned} \tag{C.4}$$

the system (C.1) can be written in the $N - \Delta$ control analysis configuration shown in figure C1(b) by using the definition of the lower LFT, which is denoted as F_l, between P^* and K

$$N = F_l(P^*, K) = \tilde{P}_{11}^* + \tilde{P}_{12}^* K (I - \tilde{P}_{22}^* K)^{-1} \tilde{P}_{21}^*. \tag{C.5}$$

The transfer function N is expressed as

$$N = \begin{bmatrix} N_{11} & N_{12} \\ N_{21} & N_{22} \\ N_{31} & N_{32} \end{bmatrix}, \tag{C.6}$$

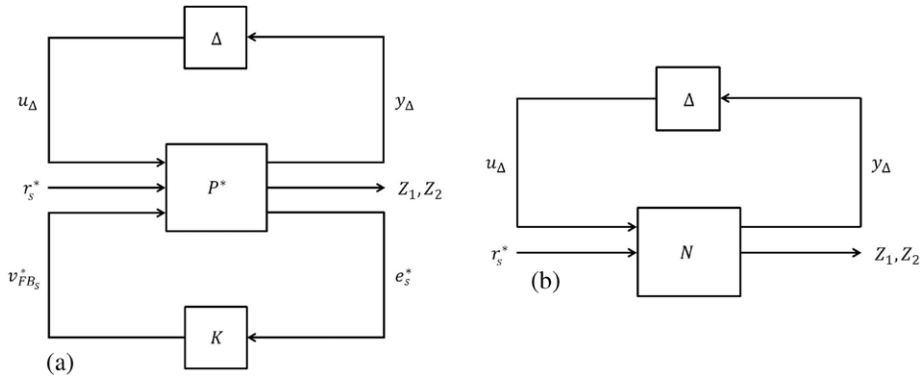

Figure C1. Model in (*a*) $\Delta - P^* - K$ robust control design framework and (*b*) $N - \Delta$ control analysis configuration.

where

$$\begin{aligned} N_{11} &= P_{11} - T_{y_\Delta v} K (I + G_{\mathrm{DC}} K)^{-1} T_{y u_\Delta}, \\ N_{12} &= T_{y_\Delta v} K (I + G_{\mathrm{DC}} K)^{-1}, \\ N_{21} &= W_{\mathrm{p}} (G_{\mathrm{DC}} K (I + G_{\mathrm{DC}} K)^{-1} - I) T_{y u_\Delta}, \\ N_{22} &= W_{\mathrm{p}} (I - G_{\mathrm{DC}} K (I + G_{\mathrm{DC}} K)^{-1}), \\ N_{31} &= -W_{\mathrm{u}} K (I + G_{\mathrm{DC}} K)^{-1} T_{y u_\Delta}, \\ N_{32} &= W_{\mathrm{u}} K (I + G_{\mathrm{DC}} K)^{-1} \end{aligned} \tag{C.7}$$

and

$$\begin{aligned} G_{\mathrm{DC}} &= \Sigma_{\mathrm{s}}^{-1} U_{\mathrm{s}}^{\mathrm{T}} Q^{1/2} P_{22} R^{-1/2} V_{\mathrm{s}}, \\ T_{y_\Delta v} &= P_{12} R^{-1/2} V_{\mathrm{s}}, \\ T_{y u_\Delta} &= \Sigma_{\mathrm{s}}^{-1} U_{\mathrm{s}}^{\mathrm{T}} Q^{1/2} P_{21}. \end{aligned} \tag{C.8}$$

By using the definitions

$$\begin{aligned} S_{\mathrm{DC_o}} &= (I + G_{\mathrm{DC}} K)^{-1}, \\ T_{\mathrm{DC_o}} &= G_{\mathrm{DC}} K (I + G_{\mathrm{DC}} K)^{-1}, \\ I &= S_{\mathrm{DC_o}} + T_{\mathrm{DC_o}}, \end{aligned} \tag{C.9}$$

where $S_{\mathrm{DC_o}}$ is the decoupled output sensitivity function and $T_{\mathrm{DC_o}}$ is the decoupled output complementary sensitivity function, (C.6) is written as

$$N = \begin{bmatrix} P_{11} - T_{y_\Delta v} K S_{\mathrm{DC_o}} T_{y u_\Delta} & T_{y_\Delta v} K S_{\mathrm{DC_o}} \\ -W_{\mathrm{p}} S_{\mathrm{DC_o}} T_{y u_\Delta} & W_{\mathrm{p}} S_{\mathrm{DC_o}} \\ -W_{\mathrm{u}} K S_{\mathrm{DC_o}} T_{y u_\Delta} & W_{\mathrm{u}} K S_{\mathrm{DC_o}} \end{bmatrix}. \tag{C.10}$$

The closed-loop system is now expressed as

$$\begin{bmatrix} y_\Delta \\ Z_1 \\ Z_2 \end{bmatrix} = N \begin{bmatrix} u_\Delta \\ r_{\mathrm{s}}^* \end{bmatrix} \tag{C.11}$$

and the nominal performance condition of the closed-loop system is given by (53).

Appendix D. Interfacing feedback controller with available rtEFIT measurements

The coordinate transformation algorithm in the DIII-D PCS is employed to construct the magnetic profiles available for real-time feedback control on the normalized effective minor radius spatial domain $\hat{\rho}$ from the data provided by the real-time EFIT (rtEFIT) equilibrium reconstruction code. The measurements that are available in real-time on the normalized flux spatial domain ψ_{n} are shown in table D1. The normalized flux ψ_{n} is defined as

Table D1. Measurements available in real-time.

Measurement	Description	Units
$q(\psi_{\mathrm{n}}^{\mathrm{rt}})$	Safety factor on normalized flux spatial domain	None
ψ_{axis}	Poloidal stream function on magnetic axis	Wb rad^{-1}
ψ_{bdry}	Poloidal stream function on plasma boundary	Wb rad^{-1}
I	Plasma current	MA

$$\psi_{\mathrm{n}} = \frac{\psi - \psi_{\mathrm{axis}}}{\psi_{\mathrm{bdry}} - \psi_{\mathrm{axis}}}. \tag{D.1}$$

The safety factor $q(\psi_{\mathrm{n}}^{\mathrm{rt}})$ is provided by rtEFIT at 64 evenly spaced points

$$\psi_{\mathrm{n}}^{\mathrm{rt}} = 0, 1/64, 2/64, \ldots, 63/64. \tag{D.2}$$

We begin the magnetic profile construction algorithm by determining the normalized effective minor radius coordinates associated with the rtEFIT normalized flux coordinates (D.2).

D.1. Computing normalized effective minor radius coordinates

The basic definition of the safety factor is

$$q = -\frac{\mathrm{d}\Phi}{\mathrm{d}\Psi} = -\frac{\mathrm{d}\Phi}{2\pi\,\mathrm{d}\psi}, \tag{D.3}$$

which we use to calculate the toroidal flux coordinates $\Phi(\psi_{\mathrm{n}}^{\mathrm{rt}})$ corresponding to the values of $q(\psi_{\mathrm{n}}^{\mathrm{rt}})$ provided by rtEFIT. By using the relationship

$$\mathrm{d}\psi = (\psi_{\mathrm{bdry}} - \psi_{\mathrm{axis}})\mathrm{d}\psi_{\mathrm{n}} \tag{D.4}$$

we integrate (D.3) to obtain

$$\int_{\psi_{\rm axis}}^{\psi} \mathrm{d}\Phi = \Phi(\psi) - \Phi(\psi_{\rm axis}) = -2\pi \int_{\psi_{\rm axis}}^{\psi} q(\psi)\mathrm{d}\psi,$$

$$\Phi(\psi_{\rm n}) - \Phi(0) = -2\pi \int_{0}^{\psi_{\rm n}} (\psi_{\rm bdry} - \psi_{\rm axis}) q(\psi_{\rm n})\mathrm{d}\psi_{\rm n},$$

$$\Phi(\psi_{\rm n}) = -2\pi \int_{0}^{\psi_{\rm n}} (\psi_{\rm bdry} - \psi_{\rm axis}) q(\psi_{\rm n})\mathrm{d}\psi_{\rm n}, \tag{D.5}$$

where $\Phi(0) = 0$ by definition. By numerically integrating the right-hand side of (D.5) by employing trapezoidal integration, we compute the toroidal flux coordinates $\Phi(\psi_{\rm n}^{\rm rt}|_k)$, $2 \leqslant k \leqslant 64$, as

$$\begin{aligned}\Phi(\psi_{\rm n}^{\rm rt}|_k) &= \frac{2\pi(\psi_{\rm axis} - \psi_{\rm bdry})}{2}\frac{1}{64}\sum_{j=2}^{k}\left[q(\psi_{\rm n}^{\rm rt}|_{j-1}) + q(\psi_{\rm n}^{\rm rt}|_j)\right] \\ &= \Phi(\psi_{\rm n}^{\rm rt}|_{k-1}) + \frac{2\pi(\psi_{\rm axis} - \psi_{\rm bdry})}{2}\frac{1}{64} \\ &\quad \times \left[q(\psi_{\rm n}^{\rm rt}|_{k-1}) + q(\psi_{\rm n}^{\rm rt}|_k)\right],\end{aligned} \tag{D.6}$$

where $\Phi(\psi_{\rm n}^{\rm rt}|_1) = 0$. Because the safety factor is not computed at the plasma boundary by rtEFIT, we employ the approximation $q(\psi_{\rm n}^{\rm rt}|_{65}) = q(\psi_{\rm n}^{\rm rt}|_{64})$ to compute Φ at the plasma boundary. This approximation results in

$$\Phi(\psi_{\rm n}^{\rm rt}|_{65}) = \Phi(\psi_{\rm n}^{\rm rt}|_{64}) + 2\pi(\psi_{\rm axis} - \psi_{\rm bdry})\frac{1}{64}q(\psi_{\rm n}^{\rm rt}|_{64}). \tag{D.7}$$

By using the relationship between the toroidal flux coordinates and the mean effective minor radius ρ

$$\Phi = \pi B_{\phi,0}\rho^2, \tag{D.8}$$

where $B_{\phi,0}$ is the reference toroidal magnetic field at the geometric major radius of the tokamak, we calculate the mean effective minor radius $\rho(\psi_{\rm n}^{\rm rt}|_k)$, $1 \leqslant k \leqslant 65$, as

$$\rho(\psi_{\rm n}^{\rm rt}|_k) = \sqrt{\frac{\Phi(\psi_{\rm n}^{\rm rt}|_k)}{\pi B_{\phi,0}}}. \tag{D.9}$$

The normalized effective minor radius $\hat{\rho}(\psi_{\rm n}^{\rm rt}|_k)$, $1 \leqslant k \leqslant 65$, is then computed as

$$\hat{\rho}(\psi_{\rm n}^{\rm rt}|_k) = \frac{\rho(\psi_{\rm n}^{\rm rt}|_k)}{\rho(\psi_{\rm n}^{\rm rt}|_{65})}. \tag{D.10}$$

We now know the normalized effective minor radius coordinates associated with the rtEFIT normalized flux coordinates (D.2), which we use to construct the magnetic profiles available for real-time control on the desired spatial domain.

D.2. Constructing magnetic profiles available for real-time control

Due to the unique relationship between the normalized effective minor radius coordinates (D.10) and the rtEFIT normalized flux coordinates (D.2), we can construct the desired magnetic profiles available for real-time control shown in table D2 from the measurements $q(\psi_{\rm n}^{\rm rt})$ provided by rtEFIT.

Table D2. Magnetic profiles available in real-time.

Profile	Description (On normalized effective minor radius domain)	Units
$q(\hat{\rho})$	Safety factor	None
$i(\hat{\rho})$	Rotational transform	None
$\Psi(\hat{\rho})$	Poloidal flux	Wb
$\theta(\hat{\rho}) = \partial\psi/\partial\hat{\rho}$	Poloidal flux gradient	Wb rad^{-1}

D.2.1. Safety factor profile: q. The safety factor profile $q(\hat{\rho}(\psi_{\rm n}^{\rm rt}|_k))$, $1 \leqslant k \leqslant 64$, is computed as

$$q(\hat{\rho}(\psi_{\rm n}^{\rm rt}|_k)) = q(\psi_{\rm n}^{\rm rt}|_k). \tag{D.11}$$

As the safety factor is not computed at the plasma boundary by rtEFIT, we employ the approximation

$$q(\hat{\rho}(\psi_{\rm n}^{\rm rt}|_{65})) = q(\psi_{\rm n}^{\rm rt}|_{64}) \tag{D.12}$$

to compute the safety factor at the plasma boundary.

D.2.2. Rotational transform profile: i. The rotational transform profile is defined as $i = 1/q$, therefore, $i(\hat{\rho}(\psi_{\rm n}^{\rm rt}|_k))$, $1 \leqslant k \leqslant 64$, is computed as

$$i(\hat{\rho}(\psi_{\rm n}^{\rm rt}|_k)) = \frac{1}{q(\psi_{\rm n}^{\rm rt}|_k)}. \tag{D.13}$$

As the safety factor is not computed at the plasma boundary by rtEFIT, we employ the approximation

$$i(\hat{\rho}(\psi_{\rm n}^{\rm rt}|_{65})) = \frac{1}{q(\psi_{\rm n}^{\rm rt}|_{64})} \tag{D.14}$$

to compute the rotational transform at the plasma boundary.

D.2.3. Poloidal flux profile: Ψ. The relationship between the poloidal flux Ψ and the poloidal stream function ψ is

$$\Psi = 2\pi\psi. \tag{D.15}$$

Therefore, we use (D.1) and (D.2) to compute the poloidal flux profile $\Psi(\hat{\rho}(\psi_{\rm n}^{\rm rt}|_k))$, $1 \leqslant k \leqslant 65$, as

$$\Psi(\hat{\rho}(\psi_{\rm n}^{\rm rt}|_k)) = 2\pi\left(\psi_{\rm axis} + \frac{k-1}{64}(\psi_{\rm bdry} - \psi_{\rm axis})\right). \tag{D.16}$$

D.2.4. Poloidal flux gradient profile: θ. By using the definition of the safety factor (D.3), the relationship between Φ and ρ (D.8), and the definition of the normalized effective minor radius (D.10), the safety factor can be expressed as

$$q = -\frac{B_{\phi,0}\rho_b\rho}{\theta}. \tag{D.17}$$

Therefore, the poloidal flux gradient profile $\theta(\hat{\rho}(\psi_{\rm n}^{\rm rt}|_k))$, $1 \leqslant k \leqslant 64$, is computed as

$$\theta(\hat{\rho}(\psi_{\rm n}^{\rm rt}|_k)) = -\frac{B_{\phi,0}\rho(\psi_{\rm n}^{\rm rt}|_{65})\rho(\psi_{\rm n}^{\rm rt}|_k)}{q(\psi_{\rm n}^{\rm rt}|_k)}. \tag{D.18}$$

If (D.18) is used to compute θ at the plasma boundary, the construction algorithm will fail because of the approximation $q(\psi_n^{rt}|_{65}) = q(\psi_n^{rt}|_{64})$. In order to overcome this construction failure at the plasma boundary, the constructed poloidal flux gradient at the plasma boundary is computed as

$$\theta(\hat{\rho}(\psi_n^{rt}|_{65})) = -k_3 I, \tag{D.19}$$

where k_3 is defined in (9). This definition is consistent with the boundary conditions (8) of the magnetic diffusion equation model of the poloidal flux profile evolution in the tokamak.

D.3. Computing selected magnetic profile

The selected magnetic profile is denoted as $y_M(\hat{\rho}(\psi_n^{rt}))$. The spatial domain that the magnetic profile can be controlled on in real-time is 20 evenly spaced points

$$\hat{\rho} = 0.05, 0.1, 0.15, \ldots, 1. \tag{D.20}$$

Therefore, to complete the magnetic profile construction algorithm, the selected magnetic profile $y_M(\hat{\rho}(\psi_n^{rt}))$ is interpolated onto the spatial domain (D.20).

References

[1] Taylor T.S. *et al* 1997 *Plasma Phys. Control. Fusion* **39** B47
[2] Laborde L. *et al* 2005 *Plasma Phys. Control. Fusion* **47** 155
[3] Moreau D. *et al* 2003 *Nucl. Fusion* **43** 870
[4] Moreau D. *et al* 2008 *Nucl. Fusion* **48** 106001
[5] Ferron J. *et al* 2006 *Nucl. Fusion* **46** L13
[6] Barana O. *et al* 2007 *Plasma Phys. Control. Fusion* **49** 947
[7] Wijnands T. *et al* 1997 *Nucl. Fusion* **37** 777
[8] Suzuki T. *et al* 2005 Recent RF experiments and application of RF waves to real-time control of safety factor profile in JT-60U *AIP Conf. Proc. (Park City, UT, USA)* pp 279–86 doi:10.1063/1.2098241
[9] Moreau D. *et al* 2011 *Nucl. Fusion* **51** 063009
[10] Ou Y. *et al* 2007 *Fusion Eng. Des.* **82** 1153
[11] Witrant E. *et al* 2007 *Plasma Phys. Control. Fusion* **49** 1075
[12] Shi W. *et al* 2012 Multivariable robust control of the plasma rotational transform profile for advanced tokamak scenarios in DIII-D *American Control Conf. Proc. (Montreal, QC, Canada)* pp 5037–42 http://ieeexplore.ieee.org/stamp/stamp.jsp?tp=&arnumber=6315411&isnumber=6314593
[13] Wehner W. *et al* 2012 Optimal feedback control of the poloidal magnetic flux profile in the DIII-D tokamak based on identified plasma response models *American Control Conf. Proc. (Montreal, QC, Canada)* pp 5049–54 http://ieeexplore.ieee.org/stamp/stamp.jsp?tp=&arnumber=6315581&isnumber=6314593
[14] Wolf R.C. 2003 *Plasma Phys. Control. Fusion* **45** R1
[15] Xu C. *et al* 2010 *IEEE Trans. Plasma Sci.* **38** 163
[16] Ou Y. *et al* 2008 *Plasma Phys. Control. Fusion* **50** 115001
[17] Hinton F.L. and Hazeltine R.D. 1976 *Rev. Mod. Phys.* **48** 239
[18] Blum J. 1989 *Numerical Simulation and Optimal Control in Plasma Physics: With Applications to Tokamaks* (Paris: Wiley)
[19] Schiesser W. 1991 *The Numerical Method of Lines: Integration of Partial Differential Equations* (San Diego, CA: Academic)
[20] Golub G. and Van Loan C.F. 1996 *Matrix Computations* 3rd edn (Baltimore, MD: Johns Hopkins University Press)
[21] Skogestad S. and Postlethwaite I. 2005 *Multivariable Feedback Control Analysis and Design* (New York: Wiley)
[22] Ferron J. *et al* 1998 *Nucl. Fusion* **38** 1055
[23] Piglowski D. *et al* 2007 *Fusion Eng. Des.* **82** 1058
[24] Schuster E. *et al* 2003 Antiwindup scheme for plasma shape control with rate and magnitude actuation constraints in the DIII-D tokamak *IEEE Conf. on Decision and Control (Maui, Hawaii, USA)* pp 4634–9 doi:10.1109/CDC.2003.1272295
[25] Walker M. *et al* 2007 *Fusion Eng. Des.* **82** 1051
[26] Barton J. *et al* 2011 *Fusion Eng. Des.* **86** 1116
[27] Packard A. 1988 Whats new with μ: structured uncertainty in multivariable control *PhD Thesis* University of California, Berkeley, CA